Title

Autophagosome development and chloroplast segmentation occur synchronously for piecemeal degradation of chloroplasts

Authors

Masanori Izumi[a,b,1], Sakuya Nakamura[a], Kohei Otomo[c,d,e,f,g], Hiroyuki Ishida[h], Jun Hidema[i], Tomomi Nemoto[c,d,e,f], Shinya Hagihara[a],

Affiliations

[a]Center for Sustainable Resource Science (CSRS), RIKEN, 351-0198 Wako, Japan
[b]Frontier Research Institute for Interdisciplinary Sciences (FRIS), Tohoku University, 980-8578 Sendai, Japan
[c]Exploratory Research Center on Life and Living Systems (ExCELLs), National Institutes of Natural Sciences, 444-8787 Okazaki, Japan
[d]National Institute for Physiological Sciences, National Institutes of Natural Sciences, 444-8787 Okazaki, Japan
[e]The Graduate University for Advanced Studies (SOKENDAI), 444-8787 Okazaki, Japan
[f]Research Institute for Electronic Science, Hokkaido University, 001-0020 Sapporo, Japan
[g]Graduate School of Medicine, Juntendo University, 113-8421 Tokyo, Japan
[h]Graduate School of Agricultural Science, Tohoku University, 980-8572 Sendai, Japan
[i]Graduate School of Life Sciences, Tohoku University, 980-8577 Sendai, Japan
[1]Address correspondence to: masanori.izumi@riken.jp

Author contributions

M.I. conceived the study. M.I. performed biochemical assays. M.I., K.O, and T.N. performed two-photon excitation microscopy observations. M.I., S.N., H.I., J.H., and S.H. performed confocal microscopy studies. M.I. wrote the manuscript with the support of all authors.

Funding

This work was supported, in part, by KAKENHI (grant numbers JP16H06280, JP18H04852, JP20H04916 to M.I., JP20H05352, JP22H04660 to S.N., JH22H04627 to H.I.), the Cooperative Research Program of "NJRC Mater. & Dev." (to M.I.), and the Joint Research by Exploratory Research Center on Life and Living Systems (ExCELLS program number 20-314 to M.I.).

Abstract

Plants distribute many nutrients to chloroplasts during leaf development and maturation. When leaves senesce or experience sugar starvation, the autophagy machinery degrades chloroplast proteins to facilitate efficient nutrient reuse. Here, we report on the intracellular dynamics of an autophagy pathway responsible for piecemeal degradation of chloroplast components. Through live-cell monitoring of chloroplast morphology, we observed the formation of chloroplast budding structures in sugar-starved leaves. The buds were then released and incorporated into the vacuolar lumen as an autophagic cargo termed a Rubisco-containing body. These budding structures did not accumulate in mutants of core autophagy machinery, suggesting that autophagosome creation is required for forming chloroplast protrusions. Simultaneous tracking of chloroplast morphology and autophagosome development revealed that the isolation membranes of autophagosomes tightly interact with part of the chloroplast surface before forming chloroplast buds. Chloroplasts then protrude at the site associated with the isolation membranes, which divide synchronously with autophagosome maturation. This autophagy-related division does not require DYNAMIN-RELATED PROTEIN 5B (DRP5B), which constitutes the division ring for chloroplast proliferation in growing leaves. An unidentified division machinery may thus fragment chloroplasts for degradation in coordination with the development of the chloroplast-associated isolation membrane.

Introduction

Organelle morphology changes dynamically in response to fluctuations in cell functions, developmental stages, and environmental cues. Plastids are plant-specific organelles that differentiate into chloroplasts in green tissues to perform photosynthesis. Plastids further serve as hubs for various metabolic pathways such as the biosynthesis of amino acids and plant hormones. Dynamic changes in plastid morphology also act as switches initiating biological programs (Osteryoung and Pyke, 2014). For instance, chloroplasts in leaf pavement cells form stroma-filled tubular extensions termed stromules to activate programed cell death as an immune response upon perception of an invading pathogen, in a process regulated by the plant hormone salicylic acid (Caplan et al., 2015).

Leaf aging is closely associated with morphological and functional changes of plastids. At the early stage of leaf development, the undifferentiated form of plastids, termed proplastids, are converted to green chloroplasts as their population expands through active division. In Arabidopsis (*Arabidopsis thaliana*), the coordination of cytoplasmic ring structures comprising DYNAMIN-RELATED PROTEIN 5B (DRP5B), also called ACCUMULATION AND REPLICATION OF CHLOROPLASTS 5 (ARC5), and intrachloroplastic ring structures consisting of FILAMENTING TEMPERATURE-SENSITIVE Z (FTSZ) proteins mediates chloroplast division (Chen et al., 2018). In mature leaves, spherical chloroplasts occupy almost all of the cytoplasm and manifest high photosynthetic activity. When older leaves later senesce, the size and number of chloroplasts gradually decrease (Martinoia et al., 1983; Mae et al., 1984). Younger leaves closer to the shoot apex will sometimes shade older leaves beneath them, thus perturbing photosynthesis by decreasing the amount of light reaching those leaves and causing local sugar starvation. In such sugar-starved leaves, senescence is accelerated to facilitate the relocation of nutrients into newly developing tissues (Weaver and Amasino, 2001; Ono et al., 2013; Law et al., 2018). Autophagy is an intracellular degradation machinery that contributes to the decline in chloroplast volume and numbers during leaf senescence (Wada et al., 2009).

Autophagy is a ubiquitous mechanism that transports cytoplasmic components to the vacuolar/lysosomal compartment for degradation in eukaryotic cells. The major autophagy pathway called macroautophagy, or simply autophagy, begins with the assembly of a membrane termed the isolation membrane (also known as a phagophore) that forms a double-membrane vesicle termed the autophagosome and sequesters a portion of the cytoplasm. Core AUTOPHAGY (ATG) proteins (ATG1–10, 12–14, 16, 18) are highly conserved among plants, yeasts, and mammals (Yoshimoto and Ohsumi, 2018; Nakamura et al., 2021a), and are required for the initiation and elongation of the isolation membrane (Nakatogawa, 2020). The outer membrane of autophagosomes fuses with the vacuolar/lysosomal membrane, resulting in the formation of autophagic bodies whose cargos are digested by vacuolar/lysosomal hydrolases. Our previous studies identified two types of autophagy for chloroplast degradation in mature leaves (Ishida et al., 2014; Nakamura and Izumi, 2018). Senescence and sugar starvation preferentially activate piecemeal degradation of chloroplast components involving a specific type of autophagic body termed a Rubisco-containing body (RCB), leading to smaller chloroplasts (Ishida et al., 2008; Wada et al., 2009; Izumi et al., 2015). The second type of autophagy, termed chlorophagy, removes entire unnecessary chloroplasts (Izumi et al., 2017; Nakamura et al., 2018), thereby modulating the number of chloroplasts in a cell (Wada et al., 2009; Izumi et al., 2017).

Mitochondria are another type of energy-producing organelle derived from endosymbiosis. Dynamin-related proteins (DRPs) also mediate mitochondrial division (Giacomello et al., 2020); the involvement of DRP-mediated organelle division in mitochondrion-targeted autophagy—termed mitophagy—in mammals and budding yeast (*Saccharomyces cerevisiae*) has been under debate (Chen et al., 2022). Drp1 and Dnm1p (Dynamin-related 1) participate in mitochondrial fission in mammals and budding yeast, respectively. Previous studies have suggested that segmented mitochondria resulting from Drp1/Dnm1p-mediated fission

become a target for degradation by autophagosomes (Twig et al., 2008; Rambold et al., 2011; Abeliovich et al., 2013). Notably, Drp1/Dnm1p-independent mitophagy has also been observed (Yamashita et al., 2016), whereby mitochondrial division occurs concomitantly with the development of the mitochondrion-associated isolation membrane, forming an autophagosome that specifically contains mitochondrial components termed the mitophagosome. A recent study identified the mitochondrial intermembrane-space protein mitofissin (also called Atg44p), required for mitochondrial fission during yeast mitophagy (Fukuda et al., 2023).

Plant autophagic bodies and RCBs are typically around 1 μm in diameter (Chiba et al., 2003; Yoshimoto et al., 2004), which is smaller than chloroplasts. Thus, piecemeal-type chloroplast autophagy via RCBs must start with division of the chloroplast segments that are to be degraded. However, how a fragment of a chloroplast can be transported to the vacuole remains poorly understood. Here, to characterize the underlying intracellular dynamics, we performed high-resolution imaging analyses in living cells of Arabidopsis leaves. Via time-lapse microscopy observations, we visualized the segmentation of chloroplast budding structures and their transport to the vacuolar lumen. Use of multiple organelle markers revealed that the development of the chloroplast-associated isolation membrane and the formation of RCBs occur simultaneously. These morphological changes did not correspond to the emergence of stromules or to DRP5b-mediated chloroplast division. Therefore, a previously undescribed chloroplast division machinery may be in play during chloroplast autophagy.

Results

Chloroplast budding structures containing stroma and envelope are released in response to sugar starvation

To observe the intracellular dynamics of the piecemeal-type of chloroplast autophagy, we subjected the mature leaves of Arabidopsis plants to incubation in darkness, as this treatment induces sugar starvation and accelerates leaf senescence, thus activating the RCB-mediated chloroplast autophagy (Izumi et al., 2010). Exogenous application of concanamycin A (concA), an inhibitor of vacuolar H^+-ATPase, allows the vacuolar accumulation of autophagic cargoes, including RCBs, facilitating their visualization (Yoshimoto et al., 2004; Ishida et al., 2008). Following the excision and incubation in darkness of leaves harboring chloroplast stroma-targeted fluorescent protein markers such as RUBISCO SMALL SUBUNIT (RBCS) fused to monomeric red fluorescent protein (mRFP) in the presence of concA, we observed the accumulation of many small vesicles containing RBCS-mRFP signal in the vacuole, i.e., RCBs (Figure 1–figure supplement 1A and 1C). Although co-incubation of dark-treated leaves with concA and mineral nutrient-rich Murashige and Skoog (MS) salts did not block the RCB accumulation, the addition of sucrose did, by rescuing the sugar-starved leaf (Figure 1–figure supplement 1A and 1C). We detected no RCBs when we subjected the leaves of a mutant for the core *ATG* gene *ATG7* to dark incubation in sucrose-free solution (Figure 1–figure supplement 1B and 1C). These observations indicate that RCBs are a type of autophagic cargo involved in the degradation of chloroplast fragments in response to sugar starvation. Therefore, in this study, we monitored chloroplast morphology in sugar-starved leaves resulting from their incubation in darkness in a sugar-free solution.

We wished to monitor the changes in the three-dimensional (3D) morphology of chloroplasts during autophagic degradation of chloroplast fragments. We thus used a two-photon excitation microscope equipped with a confocal spinning-disk unit (Otomo et al., 2015), which facilitates the monitoring of changes in the 3D cellular structures of living plant cells (Sasaki et al., 2019; Nakamura et al., 2021b). Using dark-incubated leaves from transgenic plants harboring chloroplast-targeted *GFP* (*CT-GFP*) or *RBCS-mRFP* transgenes, we determined that mesophyll chloroplasts form a type of budding structure containing stromal components (Figure 1A and 1B, arrowheads). We observed these structures budding off from their associated chloroplasts within

Fig. 1

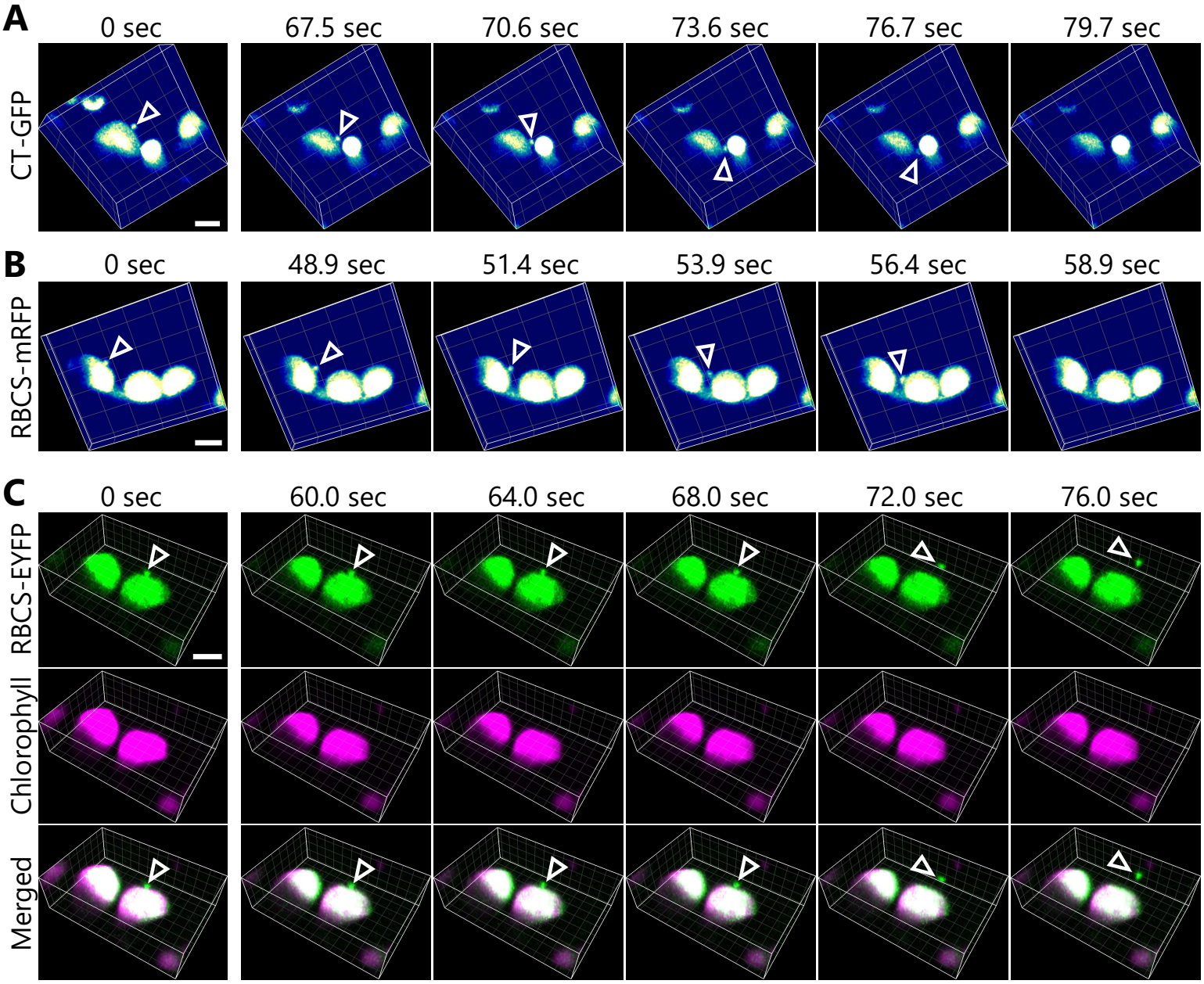

Figure 1. Chloroplast buds are released in sugar-starved leaves.
Time-lapse observations of 3D-reconstructed chloroplast morphology in Arabidopsis mesophyll cells accumulating chloroplast stroma-targeted fluorescent markers. A leaf from a plant accumulating chloroplast stroma-targeted GFP (CT-GFP) (A), RBCS-mRFP (B), or RBCS-EYFP (C) was incubated in sugar-free solution in darkness and then observed through a two-photon excitation microscope equipped with a confocal spinning disk unit. Images in (A–C) are still frames from videos 1, 2, and 3, respectively. Arrowheads indicate chloroplast budding structures. Scale bars, 5 µm. In (C), green, RBCS-EYFP; magenta, chlorophyll fluorescence. In the merged images, the overlapping regions of RBCS-EYFP and chlorophyll signals appear white.

Figure 1-figure supplement 1

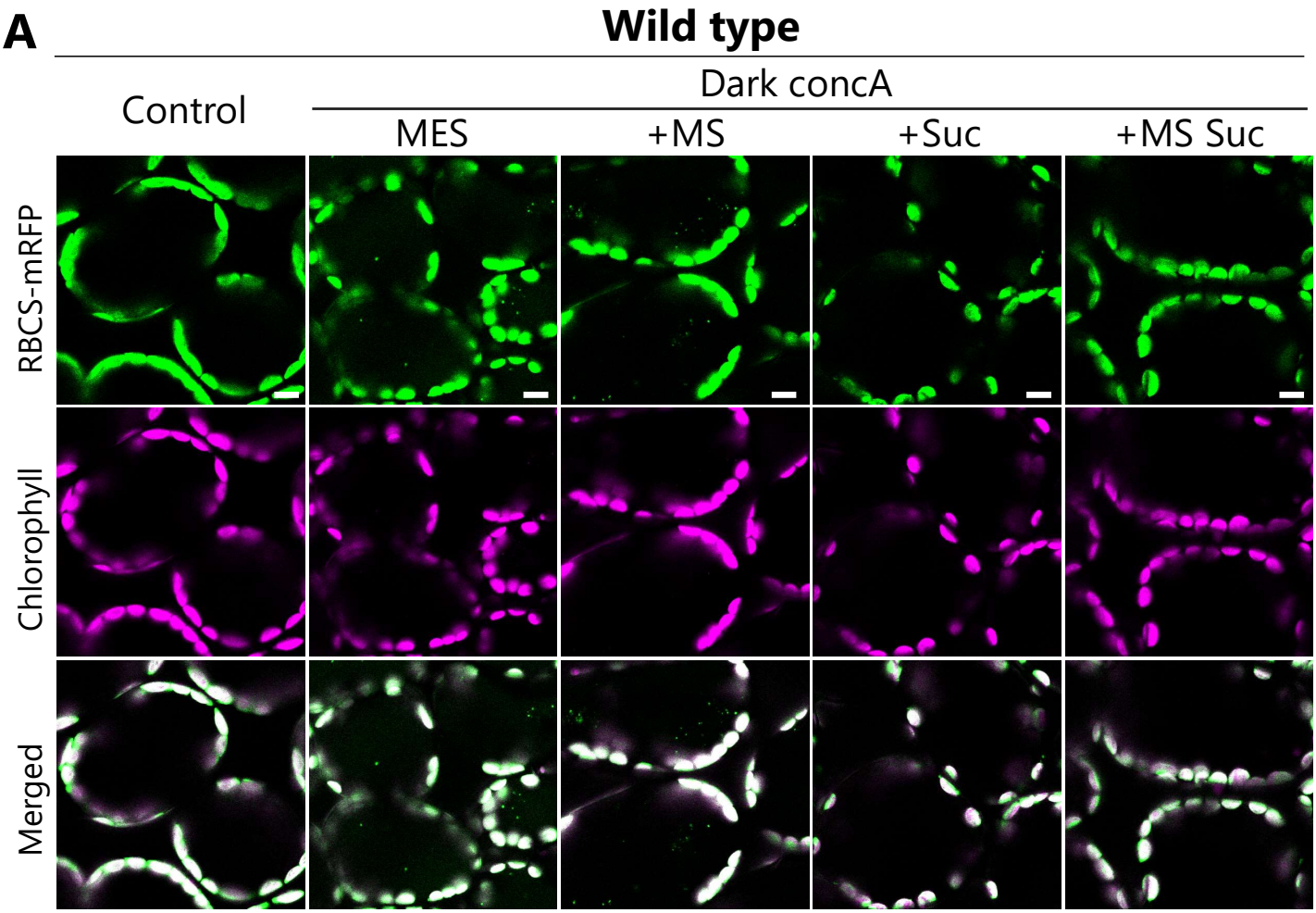

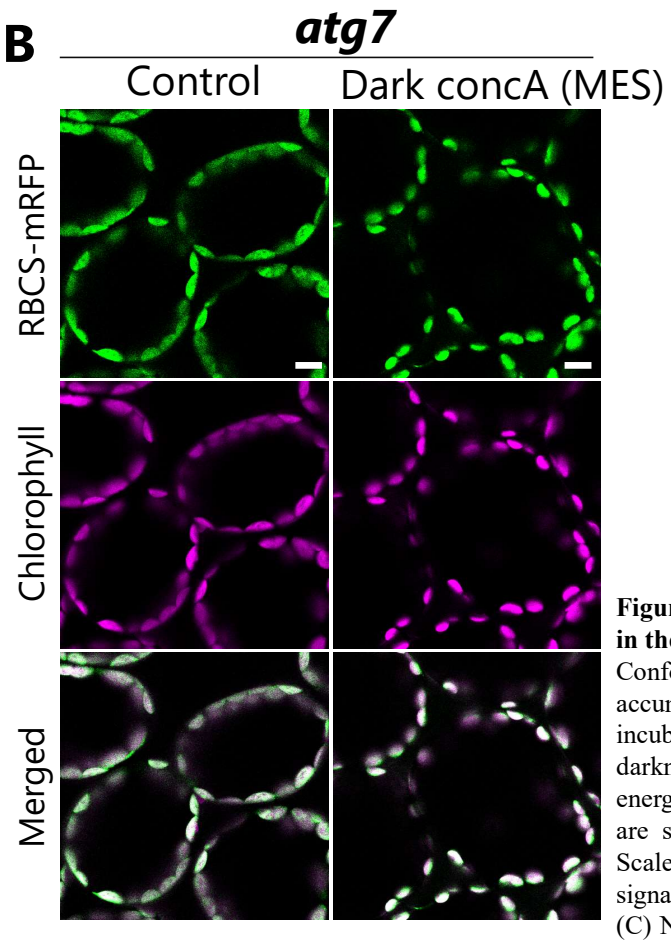

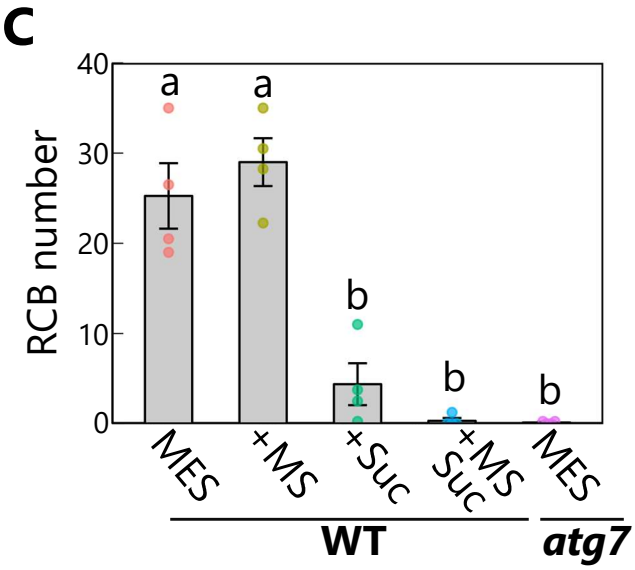

Figure 1–figure supplement 1. Accumulation of chloroplast stroma components in the vacuole via autophagy.

Confocal images of mesophyll cells from wild-type (A) or *atg7* (B) plants accumulating the chloroplast stroma marker RBCS-mRFP. The excised leaves were incubated in 10 mM MES-NaOH containing 1 μM concanamycin A (concA) in darkness. Sucrose (Suc) or Murashige and Skoog salts (MS) were added as an energy or nutrient source, respectively. Second rosette leaves from nontreated plants are shown as control. Green, RBCS-mRFP; magenta, chlorophyll fluorescence. Scale bars, 10 μm. The small vesicles containing RBCS-mRFP without chlorophyll signal appear as green and are Rubisco-containing bodies (RCBs) in the vacuole. (C) Number of accumulated RCBs from the observations described in (A) and (B). Different lowercase letters denote significant differences based on Tukey's test ($P < 0.05$). Values are means ±SE ($n = 4$). Dots represent individual data points.

a few minutes (Figure 1A and 1B, Videos 1 and 2). Dual detection of the chloroplast stromal marker RBCS fused to enhanced yellow fluorescent protein (RBCS-EYFP) and of chlorophyll autofluorescence confirmed that the budding vesicle specifically contains stroma material (EYFP positive) without any chlorophyll signal, a marker of thylakoid membrane (Figure 1C, Video 3). These time-lapse observations reveal that chloroplasts form protrusions that are released in sugar-starved leaves.

We then performed a simultaneous detection of three organelle markers by using conventional confocal microscopes to determine if the chloroplast buds contained membrane-bound proteins. Accordingly, we incubated leaves from plants accumulating the chloroplast outer-envelope marker TRANSLOCON AT THE OUTER MEMBRANE OF CHLOROPLASTS 64 (TOC64) fused to mRFP and the stromal marker RBCS-GFP in darkness as described above. Under these conditions, we observed TOC64-mRFP signal surrounding a chloroplast bud (Figure 2A, arrowheads), indicating that the budding structures contain chloroplast envelope components. We also captured the transport of an RCB with TOC64-mRFP and RBCS-GFP signals (Figure 2B, Video 4). In another set of experiments, we generated transgenic plants accumulating the thylakoid membrane marker ATP synthase gamma subunit (ATPC1) fused to tagRFP and stromal RBCS-GFP. The ATPC1-tagRFP fluorescent signal fully overlapped with that of chlorophyll autofluorescence, with both originating from the thylakoid membrane (Figure 2C and 2D). In the chloroplast budding structures, however, we detected no ATPC1-tagRFP signal, in contrast to the strong stromal RBCS-GFP signal (Figure 2C, arrowheads). In agreement with this observation, we captured a released RCB that did not contain any ATPC1-tagRFP or chlorophyll signals, but accumulated plentiful RBCS-GFP (Figure 2D, Video 5). These observations support the notion that the chloroplast buds containing stromal and envelope proteins are released as RCBs without thylakoid membranes. These live-cell imaging results are consistent with an immuno-electron-microscopy study of RCBs in wheat (*Triticum aestivum*) leaves (Chiba et al., 2003).

Vacuolar membrane dynamically interacts with chloroplast stromal components to incorporate those into the vacuolar lumen

We tracked the trafficking of RCBs in mesophyll cells further and obtained a two-dimensional (2D) sequential series of images of the release and transport of an RCB in leaves accumulating stromal CT-GFP (Figure 3A, Video 6). This time series included two phases during which the vesicle moved quickly (Figure 3B, 24.4–34.8 sec and 73.8–90.5 sec). A tracking analysis for the RCB indicated that during the early phase (24.4–34.8 sec), the vesicle moved rather smoothly in one general direction (Figure 3C, Video 6); however, during the later phase (73.8–90.5 sec), the vesicle appeared to move more randomly, akin to Brownian movement (Figure 3C, Video 6). Previous studies showed that autophagic bodies accumulating into the vacuolar lumen exhibit such random movements (Ishida et al., 2008). We conclude that the vesicle was likely released into the vacuolar lumen at around 73.8 sec (Figure 3).

We postulated that the interaction between the autophagosome and the vacuolar membrane takes place before the incorporation of RCBs into the vacuole. We thus turned our attention to the dynamics of the vacuolar membrane in transgenic plants accumulating the vacuolar membrane marker VACUOLAR H^+-PYROPHOSPHATASE 1 (VHP1) fused to mGFP (Segami et al., 2014) along with the stromal marker RBCS-mRFP (Figure 4). From one of our time-lapse imaging series, we identified a still frame of an RCB present in the cytoplasm being engulfed by the vacuolar membrane (Figure 4A, open arrowheads from 25.4–30.5 sec, Video 7). Later in the time series, we observed the opening of the part of the vacuolar membrane that had engulfed the RCB, resulting in the RCB being released into the vacuolar lumen (Figure 4A, filled arrowheads from 47.0–52.0 sec, Video 7). We captured another instance of the dynamics of the vacuolar membrane in another time series, with the vacuolar membrane first surrounding the RCB (52.6–57.4 sec) before releasing it (65.3–72.9 sec) into the vacuolar lumen (Figure 4B, Video 8). Our time-lapse imaging approach thus successfully visualized the cytoplasm-to-vacuole transport

Fig. 2

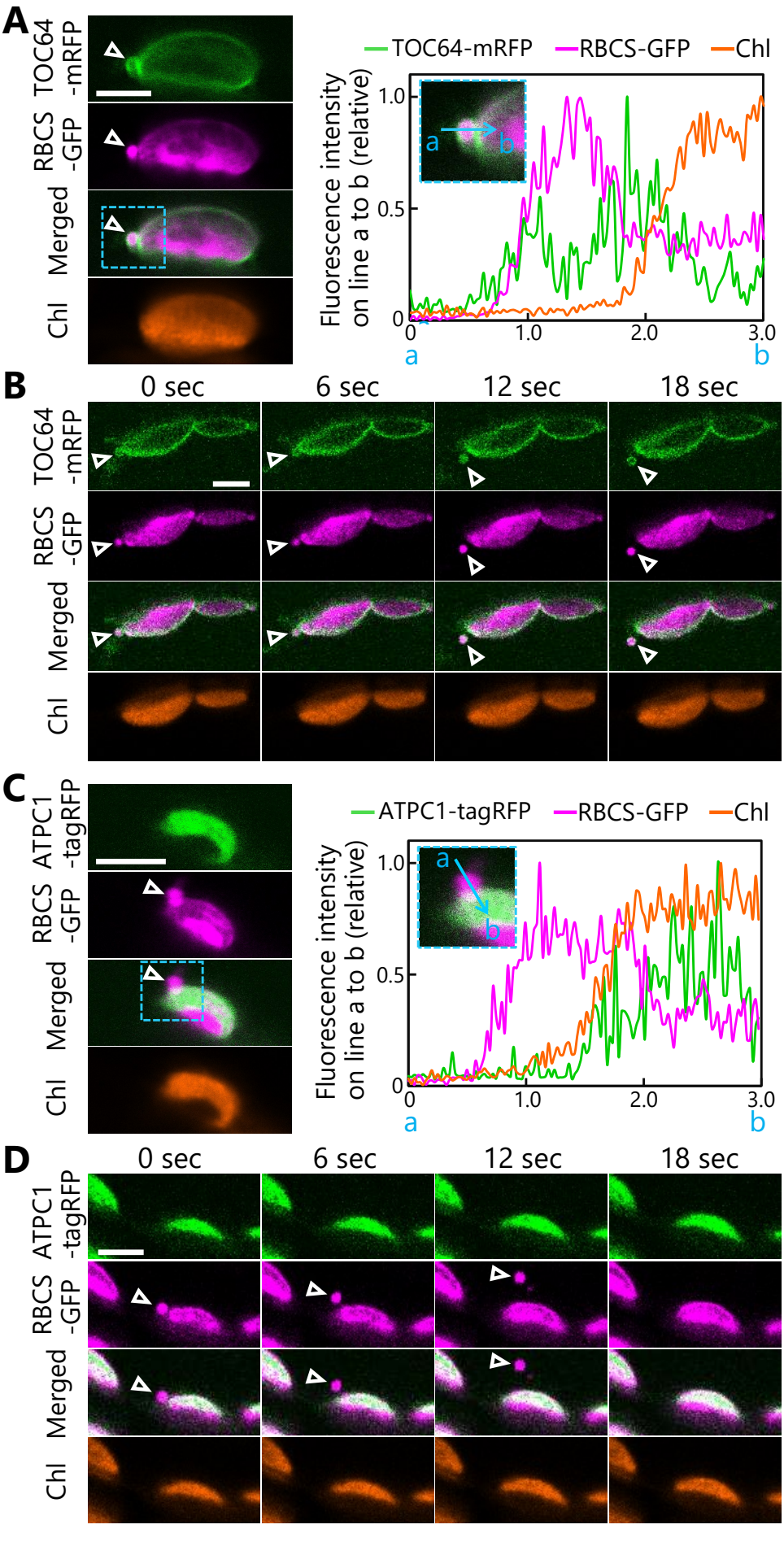

Figure 2. Chloroplast buds containing stroma and envelope components are released from the chloroplasts.

Time-lapse observations of Arabidopsis mesophyll cells accumulating the chloroplast stroma marker along with an envelope marker or a thylakoid membrane marker. Leaves accumulating stromal RBCS-GFP along with envelope-bound TOC64-mRFP (A and B) or with thylakoid membrane-bound ATPC1-tagRFP (C and D) were incubated in sugar-free solution in darkness and then observed. Images in (B) or (D) are still frames from Videos 4 and 5, respectively. Arrowheads indicate chloroplast budding structures. Scale bars, 5 µm. Green, TOC64-mRFP or ATPC1-tagRFP; magenta, RBCS-GFP; orange, chlorophyll (Chl) fluorescence. The graphs in (A and C) show fluorescence intensities along the blue lines (a to b) in the magnified images of the area indicated by dashed blue boxes. The intensities are shown relative to the maximum intensity for each fluorescence channel, set to 1.

Fig. 3

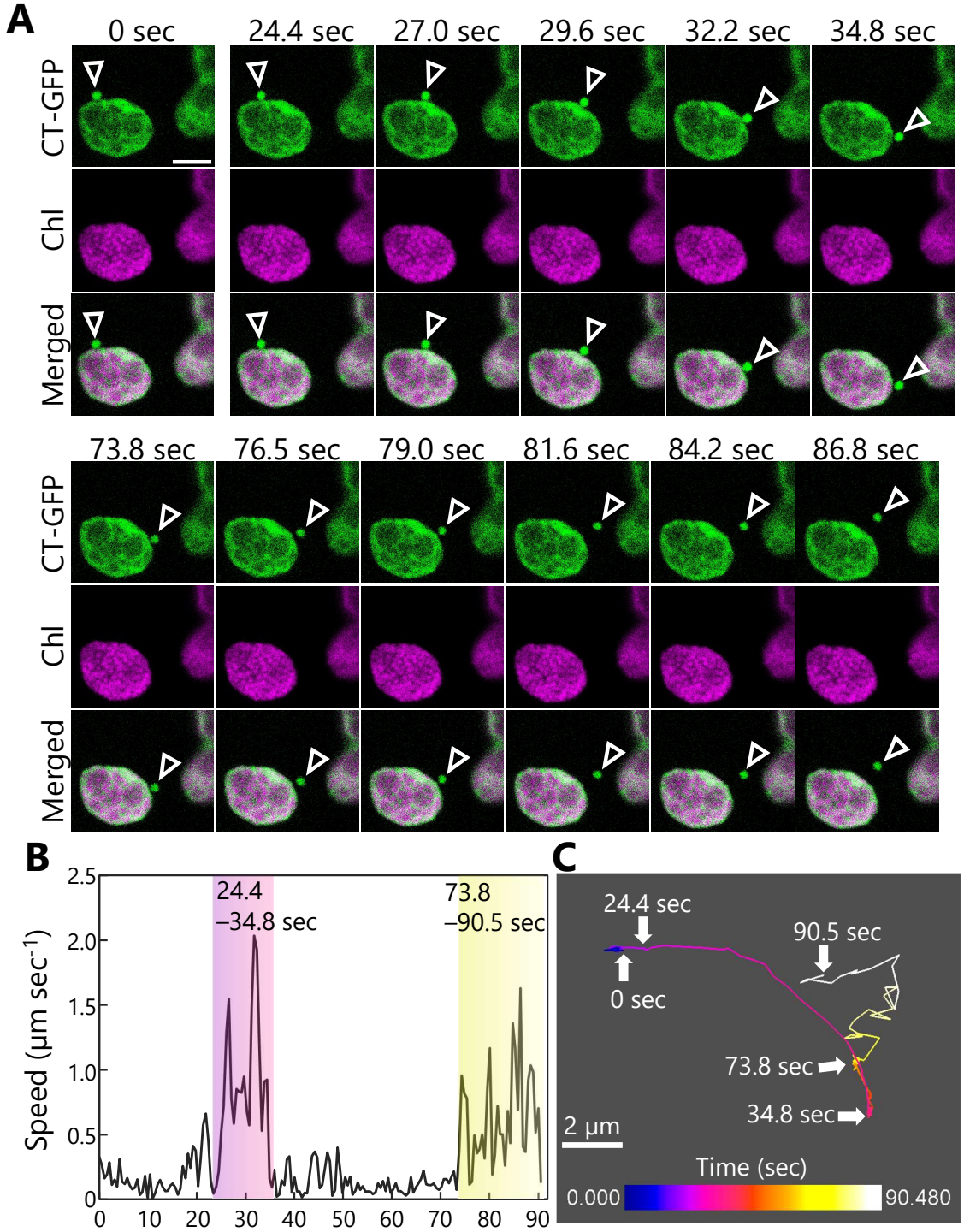

Figure 3. Tracking the transport of a Rubisco-containing body.
A leaf accumulating chloroplast-stroma targeted GFP (CT-GFP) was incubated in sugar-free solution in darkness and the transport of a Rubisco-containing body (RCB) was tracked. (A) Confocal images during the periods when the RCB moved quickly (24.4–34.8 and 73.8–90.5 sec). Arrowheads indicate an RCB. The images were generated from Video 6. Green, CT-GFP; magenta, chlorophyll (Chl) fluorescence. In the merged images, the overlapping regions of RBCS-GFP and chlorophyll signals appear white. Scale bar, 5 µm. (B) Calculated speed of the tracked RCB in (A). (C) The track of the RCB. The color of the track line changes over time, as indicated by the color bar. Scale bar, 2 µm.

Fig. 4

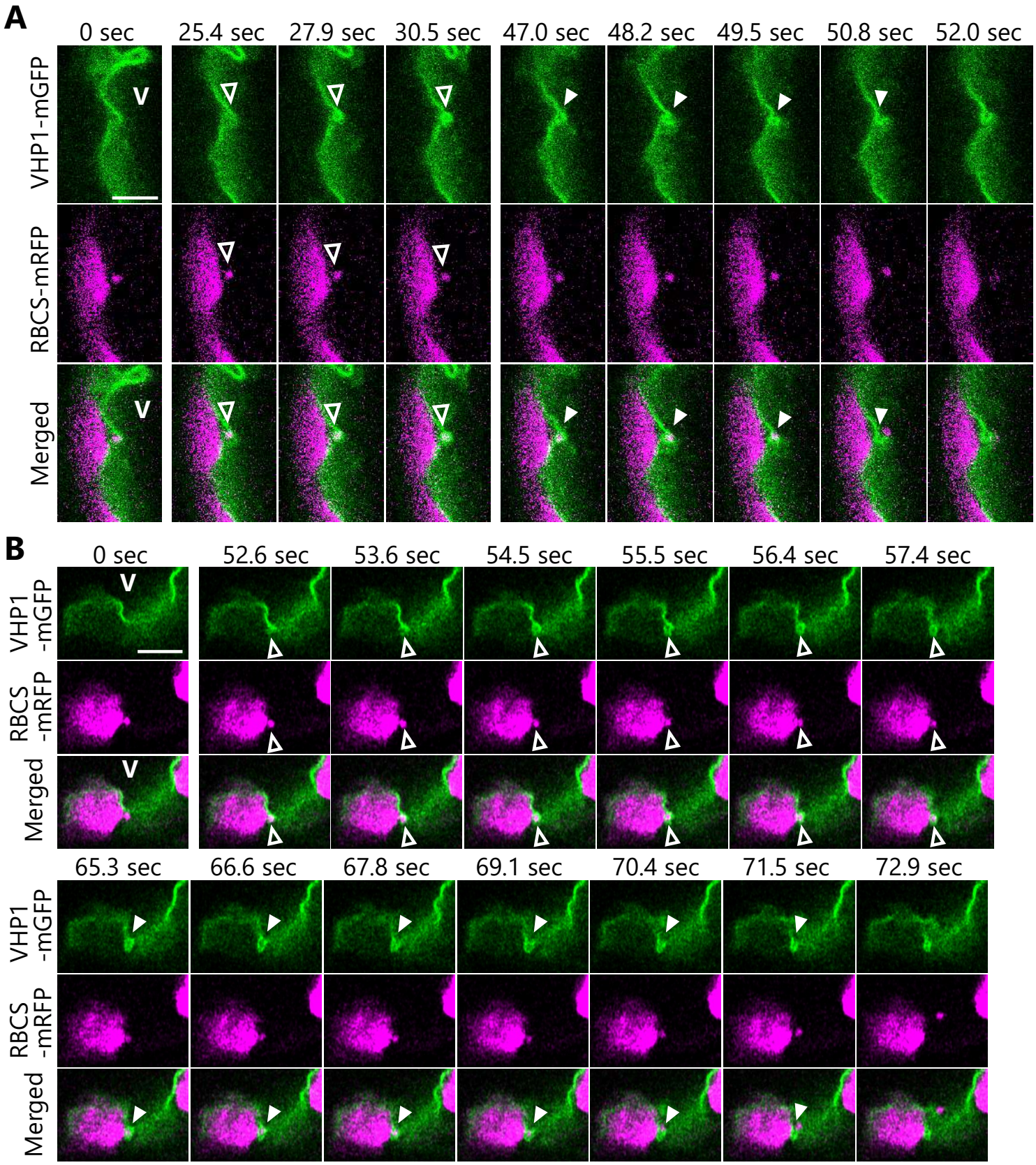

Figure 4. Dynamics of the vacuolar membrane during the incorporation of Rubisco-containing bodies.
Leaves accumulating the chloroplast stroma marker RBCS-mRFP along with the vacuolar membrane marker VHP1-mGFP were incubated in sugar-free solution in darkness and the behavior of cytosolic RCBs was monitored. The images when the vacuolar membrane engulfs an RCB (25.4–30.5 sec in A and 52.6–57.4 sec in B) and when an RCB is incorporated into the vacuolar lumen (47.0–52.0 sec in A and 65.3–72.9 in B) are shown. The images in (A) and (B) are still frames from Videos 7 and 8, respectively. Open arrowheads indicate an RCB engulfed by the vacuolar membrane. Closed arrowheads indicate the open site of the vacuolar membrane for the incorporation of an RCB. V indicates the region of the vacuolar lumen. Green, VHP1-mGFP; magenta, RBCS-mRFP. Scale bars, 5 μm.

progression of chloroplast stroma material by autophagy.

Formation and segmentation of chloroplast buds occur simultaneously with autophagosome maturation

Based on the observation of protruded structures budding off from chloroplasts (Figures 1–3), we hypothesized that these structures are formed in response to the imposed sugar starvation to be subsequently recognized and sequestered by the autophagosomal membranes. We thus expected the leaves of autophagy-deficient mutants to accumulate multiple chloroplast protrusions upon exposure to sugar starvation. This hypothesis seemed consistent with the observations of stromule-rich cells in hypocotyls or dark-incubated leaves of autophagy-deficient *atg5* or *atg7* mutants, compared with non-mutants (Ishida et al., 2008; Spitzer et al., 2015), assuming that the accumulation of chloroplast protrusions precedes stromule formation in *atg* mutants. To test this hypothesis, we subjected the leaves of *atg5* and *atg7* mutants, each defective in the function of a core ATG protein, to darkness-imposed sugar starvation and treatment with concA for 1 d (Figure 5). We detected no RCB in the leaves of either mutant (Figure 5A and 5B); however, in both the wild type and the mutants, we noticed fewer chloroplast protrusions in dark-incubated leaves treated with concA compared with the respective untreated control leaves, contrary to our hypothesis (Figure 5C and 5D). We checked single mutants of *ATG2* and *ATG10* (*atg2*, *atg10*) to investigate other core ATGs and obtained similar results (Figure 5–figure supplement 1): the number of chloroplast protrusions did not increase in *atg2* or *atg10* leaves during a 1-d incubation in darkness, and instead decreased relative to that in control leaves.

We therefore posited that autophagosome formation might be required for the production of chloroplast buds. To test this idea, we observed the behavior of autophagosomes in transgenic plants accumulating the isolation membrane marker AUTOPHAGY8a (ATG8a) fused to GFP (as GFP-ATG8a) along with stromal RBCS-mRFP or chloroplast stroma-targeted (CT)-DsRed (Figure 6). Following incubation of leaves in darkness and confocal microscopy observation, we observed isolation membranes (marked by GFP-ATG8a) that were tightly associated with the chloroplast surface before any protrusion structure was visible (Figure 6A and 6B, 0 sec). Over time, however, fluorescence monitoring of the same area revealed that the isolation-membrane-associated site from the chloroplast side gradually protruded and eventually formed a vesicle containing RBCS-mRFP or CT-DsRed and surrounded by GFP-ATG8a signal, i.e., an autophagosome (Figure 6A and 6B, arrowheads; Videos 9 and 10).

Using the time-series data shown in Figure 6B (Video 10), we evaluated the time-dependent changes of the size of the chloroplast bud and the ratio between the major axis and the minor axis of the GFP-ATG8a-labeled autophagosome (Figure 6C). This ratio drops to 1 as the isolation membrane becomes a spherical autophagosome. The ratio between the major and minor axes started to decrease at around 40 sec and approached 1 at around 100 sec. The chloroplast protrusion appeared around 50 sec and gradually increased in size until around 120 sec. These data support the notion that the chloroplast protrusion appears as the isolation membrane develops and becomes a segmented RCB when the spherical autophagosome forms. We identified another example in an independent image series (Figure 6–figure supplement 1, Video 11) where the ratio between the major and minor axes of the isolation membrane started to decrease at approximately 40 sec and the chloroplast protrusion appeared at around 50 sec. In the third set of images, we observed the formation of chloroplast buds and later of RCBs near GFP-ATG8a-associated sites on multiple chloroplasts and sequentially (Figure 6–figure supplement 2, Video 12). Therefore, we conclude that the development of the chloroplast-associated isolation membrane precedes the production of chloroplast buds and of RCBs for piecemeal-type chloroplast autophagy.

Salicylic acid influences stromule formation in autophagy-deficient mutants

Our initial hypothesis was that stromules are related to RCBs: stromule-rich cells appeared because of impaired RCB production in *atg* mutants. However, our imaging assays above revealed

Fig. 5

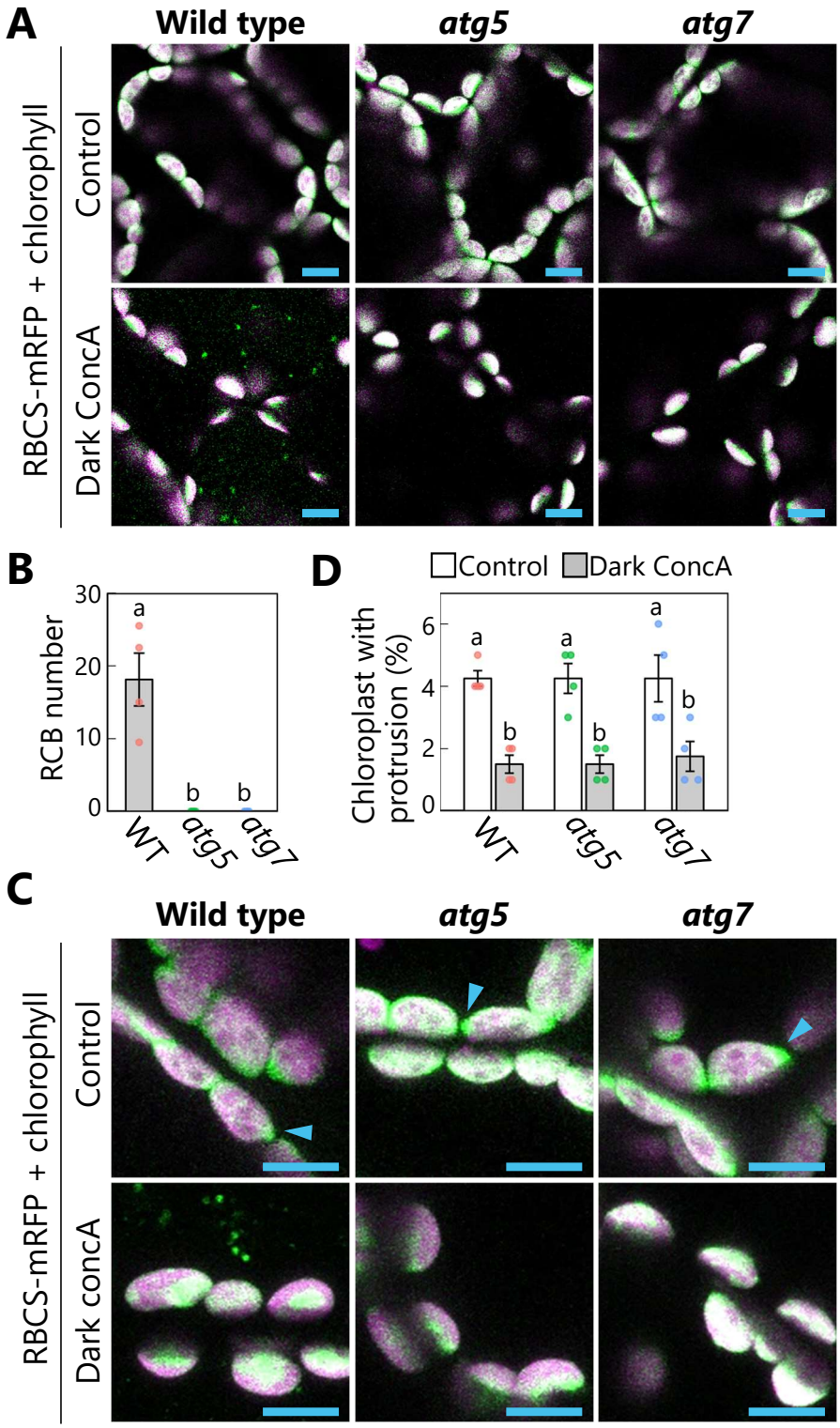

Figure 5. Autophagy deficiency does not increase the number of chloroplast protrusions during a 1-d dark treatment.
Leaves from wild-type (WT), *atg5*, or *atg7* plants accumulating the chloroplast stroma marker RBCS-mRFP were incubated in sugar-free solution containing 1 µM concanamycin A (concA) for 1 d in darkness. 2D images of mesophyll cells were acquired (A), and the number of accumulated RCBs in the vacuoles was scored (B). Leaves from untreated plants are shown as control. The appearance of chloroplast protrusions was observed from orthogonal projections created from *z*-stack images (15 µm in depth; C), and the proportion of chloroplasts having protrusion structures was calculated (D). Scale bars, 10 µm. Green, RBCS-mRFP; magenta, chlorophyll fluorescence. Only the merged channels are shown. The overlapping regions of RBCS-mRFP and chlorophyll signals appear white. Small vesicles containing RBCS-mRFP without chlorophyll signal appear as green and are RCBs in the vacuole. Arrowheads indicate the structures that were counted as a chloroplast protrusion in (D). Different lowercase letters denote significant differences based on Tukey's test ($P < 0.05$). Values are means ±SE ($n = 4$). Dots represent individual data points in each graph.

Figure 5-figure supplement 1

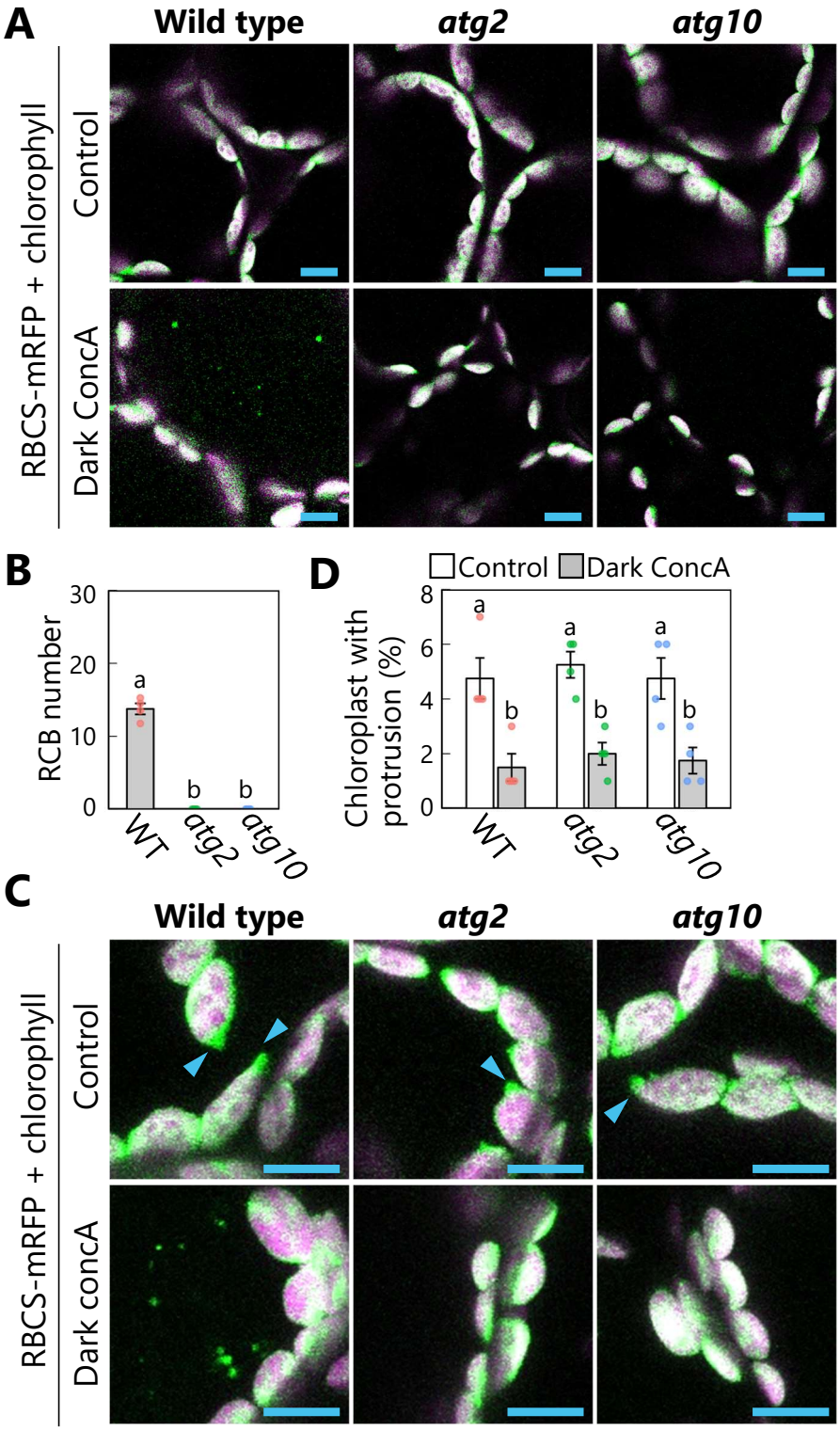

Figure 5–figure supplement 1. Chloroplast protrusions do not increase in *atg2* or *atg10* mutant leaves during a 1-d dark treatment. The experiments described in Figure 5 were performed on leaves from wild-type (WT), *atg2*, or *atg10* plants accumulating the chloroplast stroma marker RBCS-mRFP. Scale bars, 10 µm. Green, RBCS-mRFP; magenta, chlorophyll fluorescence. Only the merged channels are shown. The overlapping regions of RBCS-mRFP and chlorophyll signals appear white. Small vesicles containing RBCS-mRFP without chlorophyll signal appear as green and are RCBs in the vacuole. Arrowheads indicate the structures that were counted as a chloroplast protrusion in (D). Different lowercase letters denote significant differences based on Tukey's test ($P < 0.05$). Values are means ±SE ($n = 4$). Dots represent individual data points in each graph.

Fig. 6

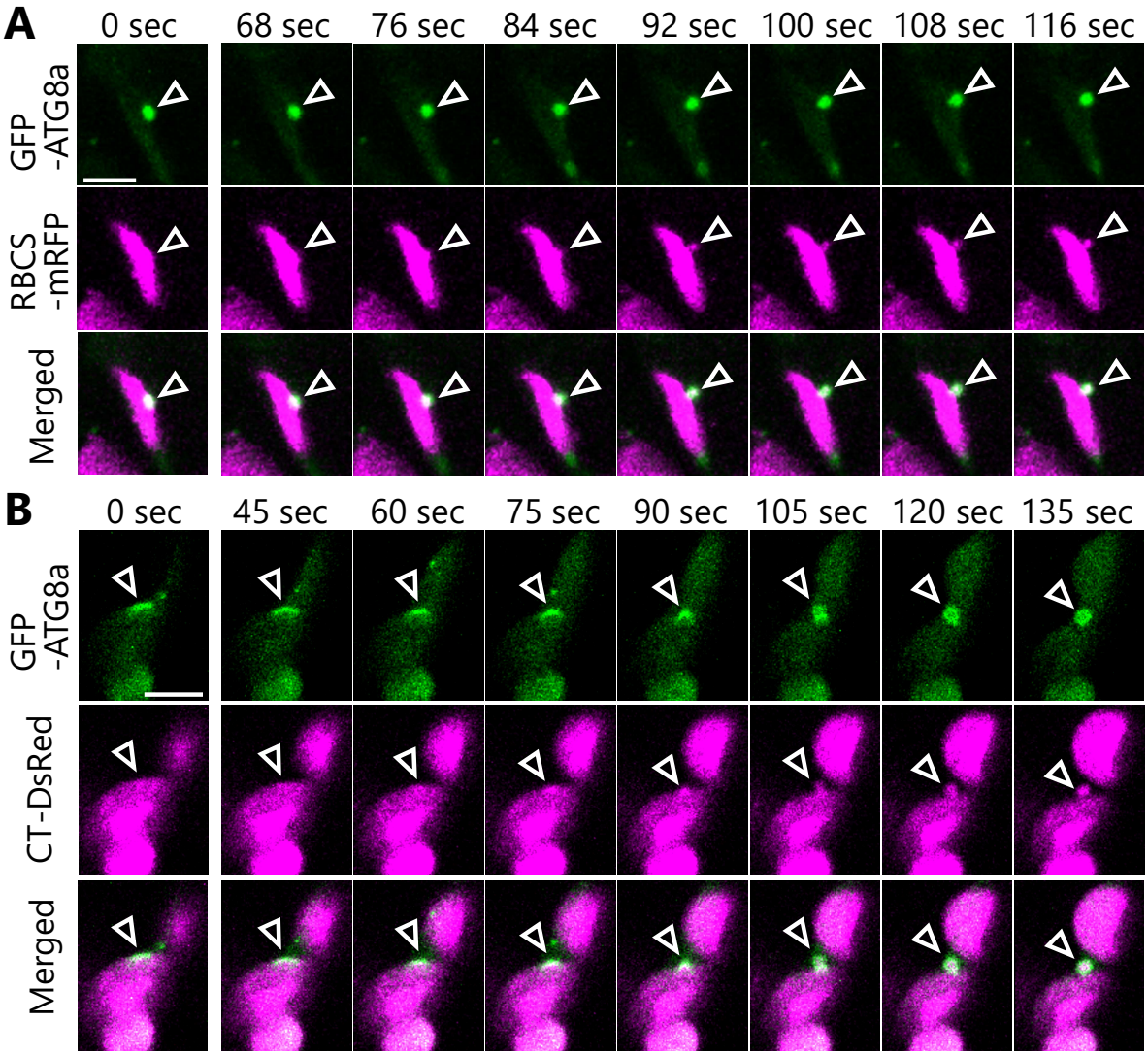

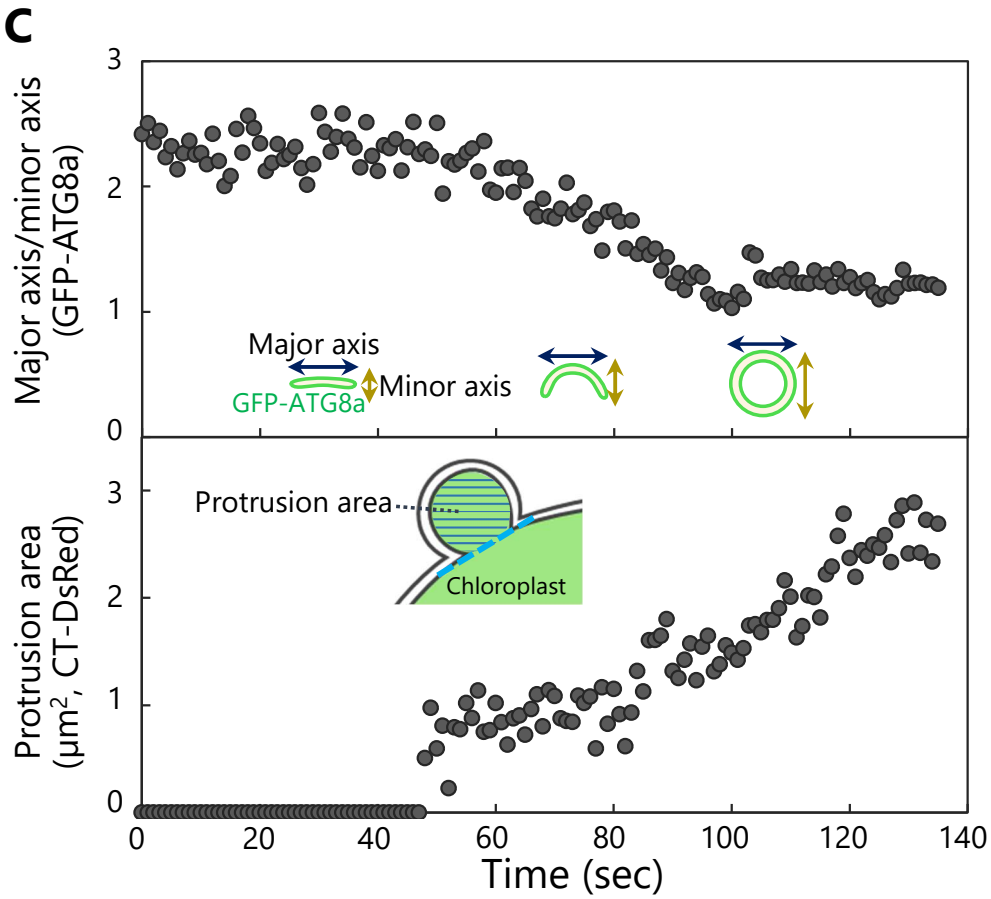

Figure 6. The formation of a chloroplast bud and the maturation of the chloroplast-associated isolation membrane occur concomitantly.
Leaves accumulating the chloroplast stroma marker, RBCS-mRFP (A) or CT-DsRed (B), and the isolation membrane marker GFP-ATG8a were incubated in sugar-free solution in darkness and then observed. Arrowheads indicate the position of the chloroplast-associated isolation membrane. Images in (A) and (B) are still frames from Videos 9 and 10, respectively. Green, GFP-ATG8a; magenta, RBCS-mRFP or CT-DsRed. Scale bars, 5 μm. (C) Time-dependent changes in the ratio of the major axis to the minor axis in the GFP-ATG8a-labeled isolation membrane (top), or in the area of the chloroplast protrusion (bottom) as measured from the images in (B).

Figure 6-figure supplement 1

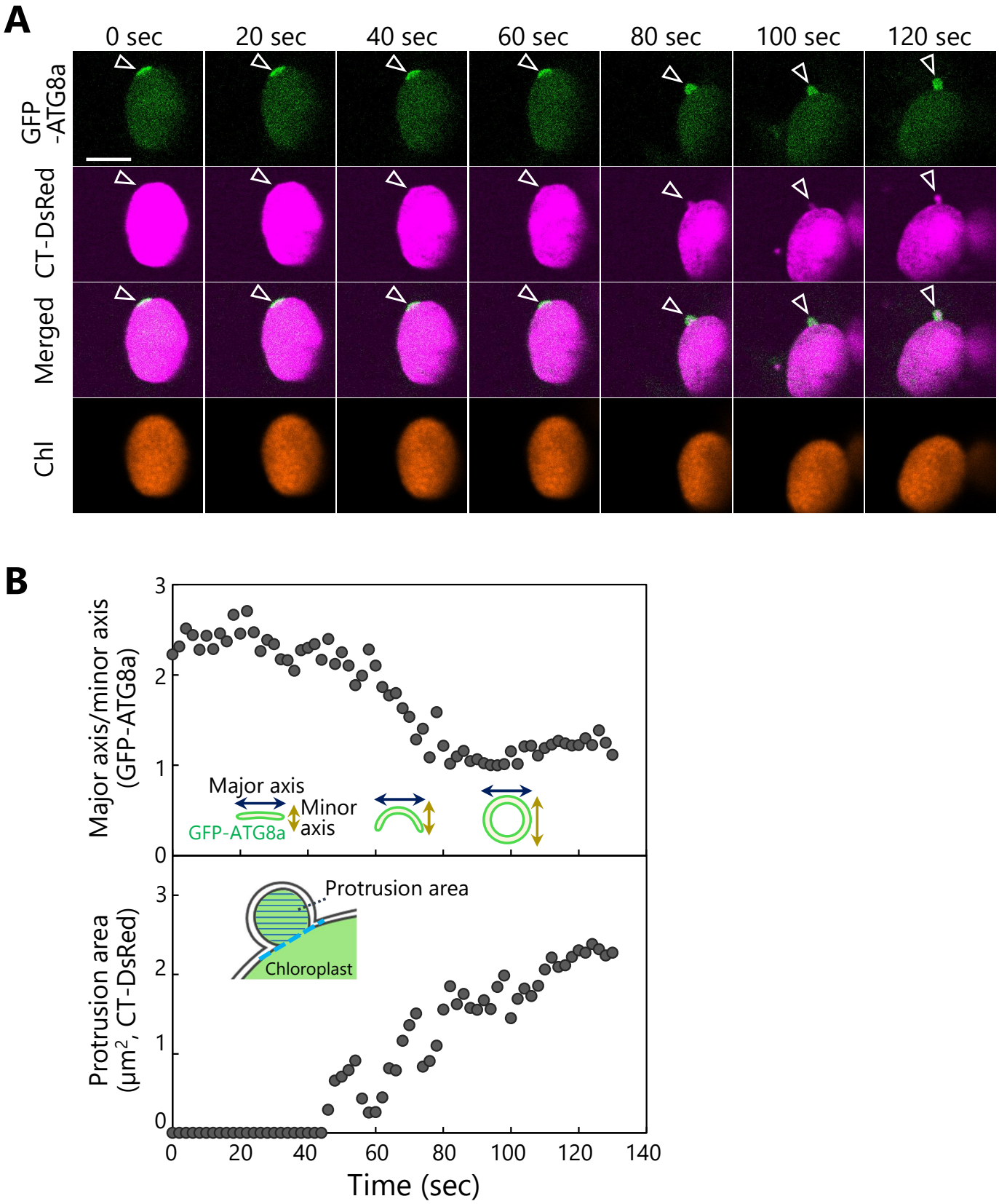

Figure 6–figure supplement 1. Another observation of the protrusion of the isolation-membrane-associated site in a chloroplast. A leaf accumulating the chloroplast stroma marker CT-DsRed and the isolation membrane marker GFP-ATG8a was incubated in sugar-free solution in darkness and then observed. Arrowheads indicate the position of the chloroplast-associated isolation membrane. The images are still frames from Video 11. Green, GFP-ATG8a; magenta, CT-DsRed. Scale bars, 5 μm. (B) Time-dependent changes in the ratio of the major axis to the minor axis in the GFP-ATG8a-labeled isolation membrane (top), or in the area of the chloroplast protrusion (bottom), as measured from the images in (A).

Figure 6-figure supplement 2

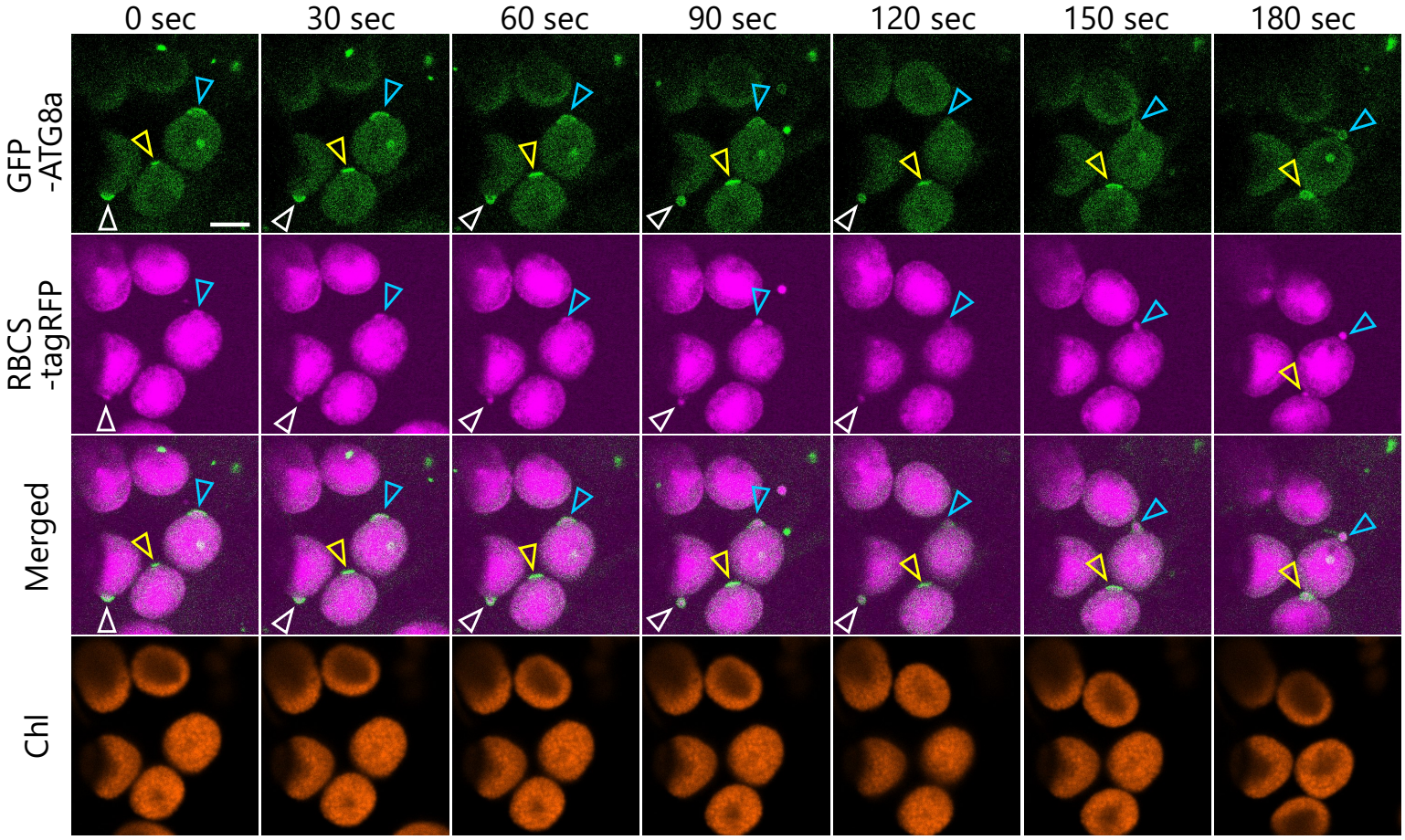

Figure 6–figure supplement 2. Chloroplast buds surrounded by the isolation membrane appear in multiple chloroplasts.
A leaf accumulating the chloroplast stroma marker RBCS-tagRFP and the isolation membrane marker GFP-ATG8a were incubated in sugar-free solution in darkness and then observed. White, yellow, or blue arrowheads indicate the isolation-membrane-associated site in different chloroplasts, respectively. The images are still frames from Video 12. Green, GFP-ATG8a; magenta, RBCS-tagRFP; orange, chlorophyll (Chl) fluorescence. Scale bars, 5 μm.

that RCBs emerge from mesophyll chloroplasts in the absence of prior stromule formation (Figure 6), pointing to the existence of another factor responsible for the elevated stromule formation seen in *atg* mutant leaves. A previous study reported the hyperaccumulation of salicylic acid (SA) in senescing Arabidopsis *atg* mutants (Yoshimoto et al., 2009). Since SA signaling stimulates immune responses, including stromule formation (Caplan et al., 2015), we speculated that SA might contribute to stromule formation in autophagy-deficient mutants. To investigate this possibility, we generated transgenic plants in the *atg5* mutant background accumulating stromal GFP (CT-GFP) and a construct carrying NahG, encoding a bacterial SA hydroxylase that catabolizes SA (Delaney, 1994; Yoshimoto et al., 2009). We examined chloroplasts in guard cells, as this cell type actively forms many more stromules than the mature chloroplasts of mesophyll cells (Ishida and Yoshimoto, 2008). Chloroplasts in the guard cells of the *atg5* mutant formed more stromules than wild-type (WT) and NahG-expressing plants (Figure 7A and 7B). Importantly, the introduction of the NahG construct into the *atg5* mutant background (*atg5* NahG) largely abolished stromule formation (Figure 7A and 7B). To further explore the role of SA in stromule formation, we generated double mutants of *SALICYLIC ACID INDUCTION DEFICIENT 2* (*SID2*), encoding the SA biosynthetic enzyme ISOCHORISMATE SYNTHASE 1, and *ATG5* or *ATG7* (*sid2 atg5* and *sid2 atg7*). The *sid2* mutation also resulted in fewer stromules in the double mutant relative to the respective *atg5* and *atg7* single mutants in guard cells (Figure 7C and 7D).

We then examined stromule formation in mesophyll chloroplasts for the same genotypes. In 20-d-old plants, we detected no stromules in any genotype (Figure 7–figure supplement 1). In cells from senescent leaves of 36-d-old plants, we observed stromules in 22.5% or 15.3% of chloroplasts from the *atg5* or *atg7* single mutants, respectively, but the introduction of the *sid2* mutation in *sid2 atg5* and *sid2 atg7* led to a decrease in the number of stromules (9.8% or 2.5% in *sid2 atg5* or *sid2 atg7*, respectively; Figure 7E and 7F). These results support the notion that SA accumulation due to autophagy deficiency activates stromule formation during leaf senescence.

The frequency of stromules was higher in the *sid2 atg5* and *sid2 atg7* double mutants than in WT plants and the *sid2* single mutant (Figure 7). We measured the content of hydrogen peroxide (H_2O_2) in all plants, since reactive oxygen species also trigger stromule formation (Caplan et al., 2015). In 36-d-old plants, *atg5* or *atg7* leaves contained 2.7 or 2.8 times more hydrogen peroxide than WT leaves (Figure 7G). Notably, the presence of the *sid2* mutation in the *sid2 atg5* and *sid2 atg7* double mutants did not alleviate hydrogen peroxide accumulation (Figure 7G). Such ROS accumulation may thus be one factor responsible for the greater number of stromules in *sid2 atg5* and *sid2 atg7* compared with WT and *sid2* plants.

DRP5b is not required for autophagy of chloroplast fragments

Simultaneous progression of autophagosome formation and organelle segmentation has been previously observed during mitophagy in mammals and budding yeast (Yamashita et al., 2016; Fukuda et al., 2023). This autophagy-related mitochondrial division does not require the mammalian Drp1- or yeast Dnm1p-dependent division machinery, respectively. Here, we examined whether the DRP5B-mediated chloroplast division participates in chloroplast autophagy and RCB production.

To this end, we generated *drp5b* mutant lines accumulating the stromal marker RBCS-mRFP or stromal GFP (CT-GFP). Although the mature leaves of *drp5b* had larger chloroplasts than WT leaves, reflective of the impaired chloroplast division during cell expansion typical of this mutant, many RCBs accumulated when the leaves were incubated in darkness in the presence of concA (Figure 8A and 8B, Figure 8–figure supplement 1). We detected no RCB in the leaves of the *drp5b atg5* double mutant (Figure 8–figure supplement 1). These results indicate that RCB-mediated chloroplast autophagy is active in the *drp5b* mutant. To obtain an independent confirmation of this result, we performed a immunoblot assay of autophagy flux, based on the

Fig. 7

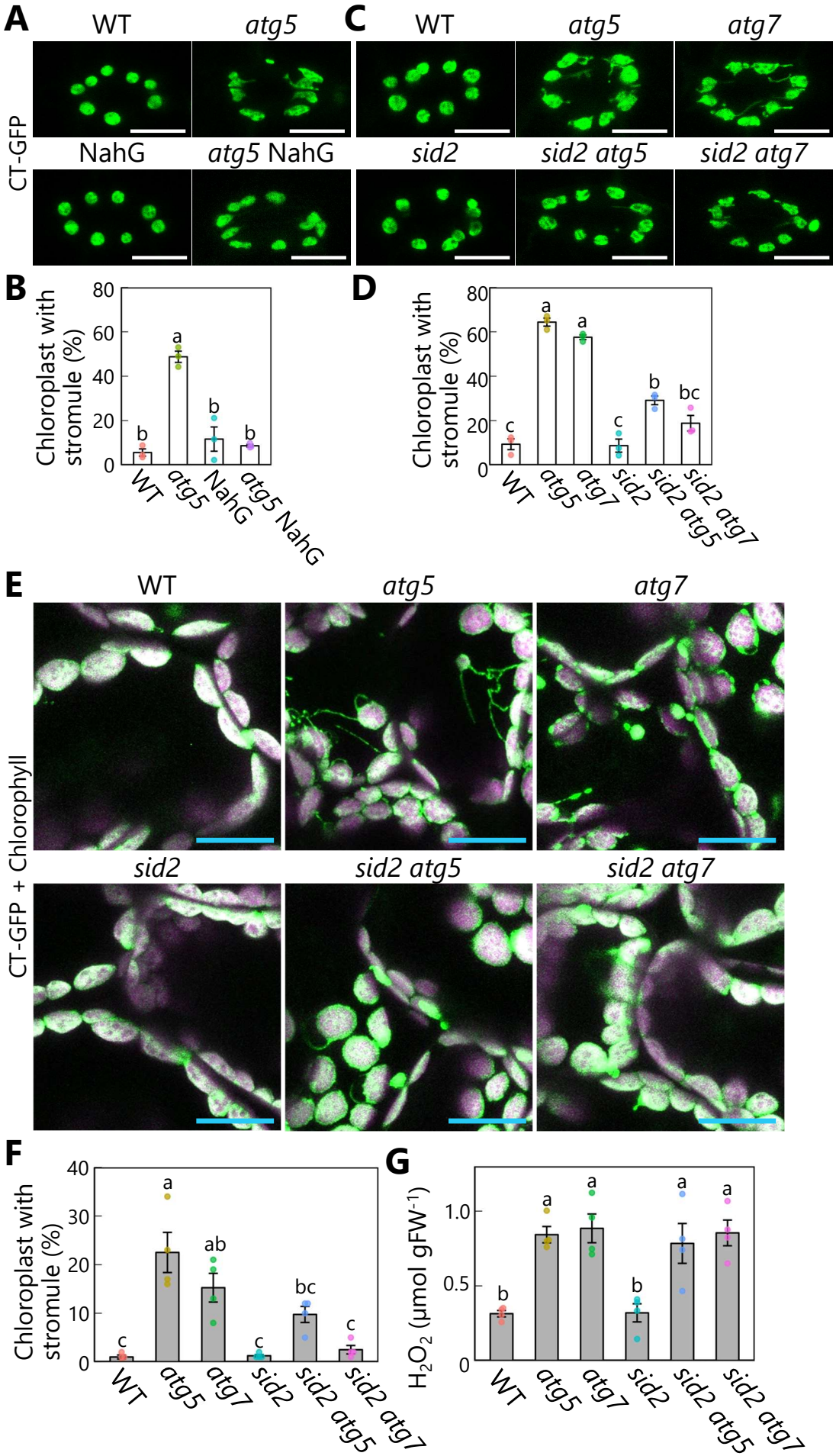

Figure 7. Diminished salicylic acid signal suppresses stromule formation in autophagy-deficient mutants.
(A) Confocal images of guard cells from wild-type (WT), *atg5*, NahG, and *atg5* NahG leaves accumulating chloroplast stroma-targeted GFP (CT-GFP). Scale bars, 10 μm. (B) Percentage of chloroplasts forming stromules, from the observations described in (A). (C) Confocal images of guard cells from WT, *atg5*, *atg7*, *sid2*, *sid2 atg5*, and *sid2 atg7* leaves accumulating CT-GFP. Scale bars, 10 μm. (D) Percentage of chloroplasts forming stromules, from the observations described in (C). In (A) and (C), orthogonal projections produced from *z*-stack images (10 μm in depth) are shown. (E) Orthogonal projections produced from *z*-stack images (15 μm in depth) of mesophyll cells from WT, *atg5*, *atg7*, *sid2*, *sid2 atg5*, and *sid2 atg7* leaves accumulating CT-GFP. Third rosette leaves from 36-d-old plants were observed. Green, CT-GFP; magenta, chlorophyll fluorescence. Only the merged channels are shown. Scale bars, 20 μm. (F) Percentage of chloroplasts forming stromules in mesophyll cells, from the observations described in (E). (G) Hydrogen peroxide (H_2O_2) content in WT, *atg5*, *atg7*, *sid2*, *sid2 atg5*, and *sid2 atg7* leaves. Different lowercase letters denote significant differences based on Tukey's test ($P < 0.05$). Values are means ±SE (n = 3 in B and D or 4 in F and G). Dots represent individual data points in each graph.

Figure 7-figure supplement 1

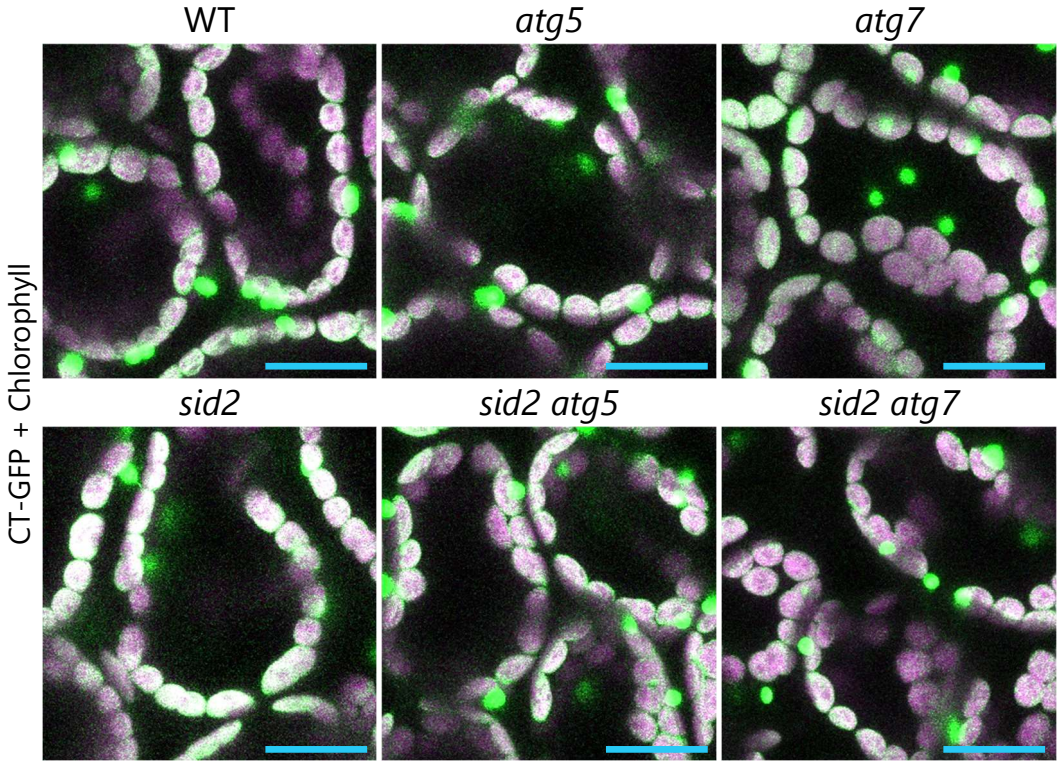

Figure 7–figure supplement 1. Autophagy deficiency does not activate stromule formation from mesophyll chloroplasts in young leaves.
Orthogonal projections produced from *z*-stack images (15 µm in depth) of mesophyll cells from WT, *atg5*, *atg7*, *sid2*, *sid2 atg5*, and *sid2 atg7* leaves accumulating CT-GFP. The third rosette leaves from 20-d-old plants were observed. Green, CT-GFP; magenta, chlorophyll fluorescence. Only the merged channels are shown. Scale bars, 20 µm.

Fig. 8

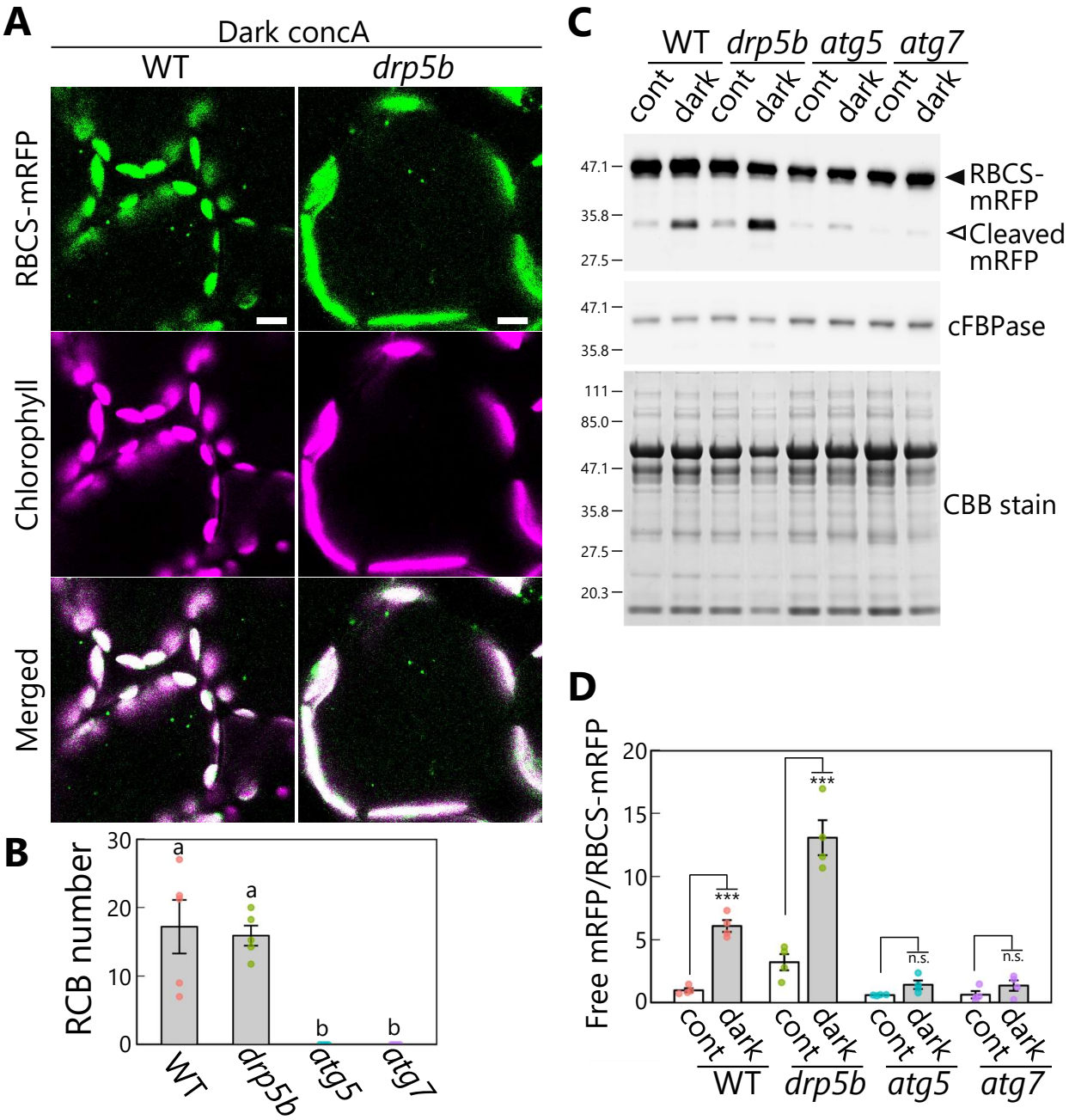

Figure 8. DRP5b is dispensable for chloroplast autophagy in sugar-starved leaves.
Confocal images of mesophyll cells from wild-type (WT) and *drp5b* leaves accumulating the stroma marker RBCS-mRFP. Second rosette leaves were incubated in sugar-free solution containing 1 µM concanamycin A (concA) in darkness. Green, RBCS-mRFP; magenta, chlorophyll fluorescence. Scale bars, 10 µm. (B) Number of accumulated RCBs in WT, *drp5b*, *atg5*, and *atg7* leaves, counted from the observations described in (A). Different lowercase letters denote significant differences based on Tukey's test ($P < 0.05$). Values are means ±SE (n = 4–5). (C) Biochemical detection of autophagy flux for chloroplast stroma based on a free RFP assay. RFP and cFBPase (loading control) were detected by immunoblotting of soluble protein extracts from leaves of WT, *drp5b*, *atg5*, and *atg7* plants accumulating RBCS-mRFP. Protein extracts from either untreated control leaves (cont) or leaves after 2 d of incubation in darkness (dark) were used. Total protein was detected by Coomassie Brilliant Blue (CBB) staining as a loading control. The filled arrowhead indicates RBCS-mRFP fusion, and the open arrowhead indicates free mRFP derived from the cleavage of RBCS-mRFP. (D) Quantification of the free mRFP/RBCS-mRFP ratio shown relative to that of untreated wild-type plants, which was set to 1. Asterisks denote significant differences based on t-test (***, $P < 0.05$; n.s., not significant). Values are means ±SE (n = 4). Dots represent individual data points in each graph.

Figure 8–figure supplement 1

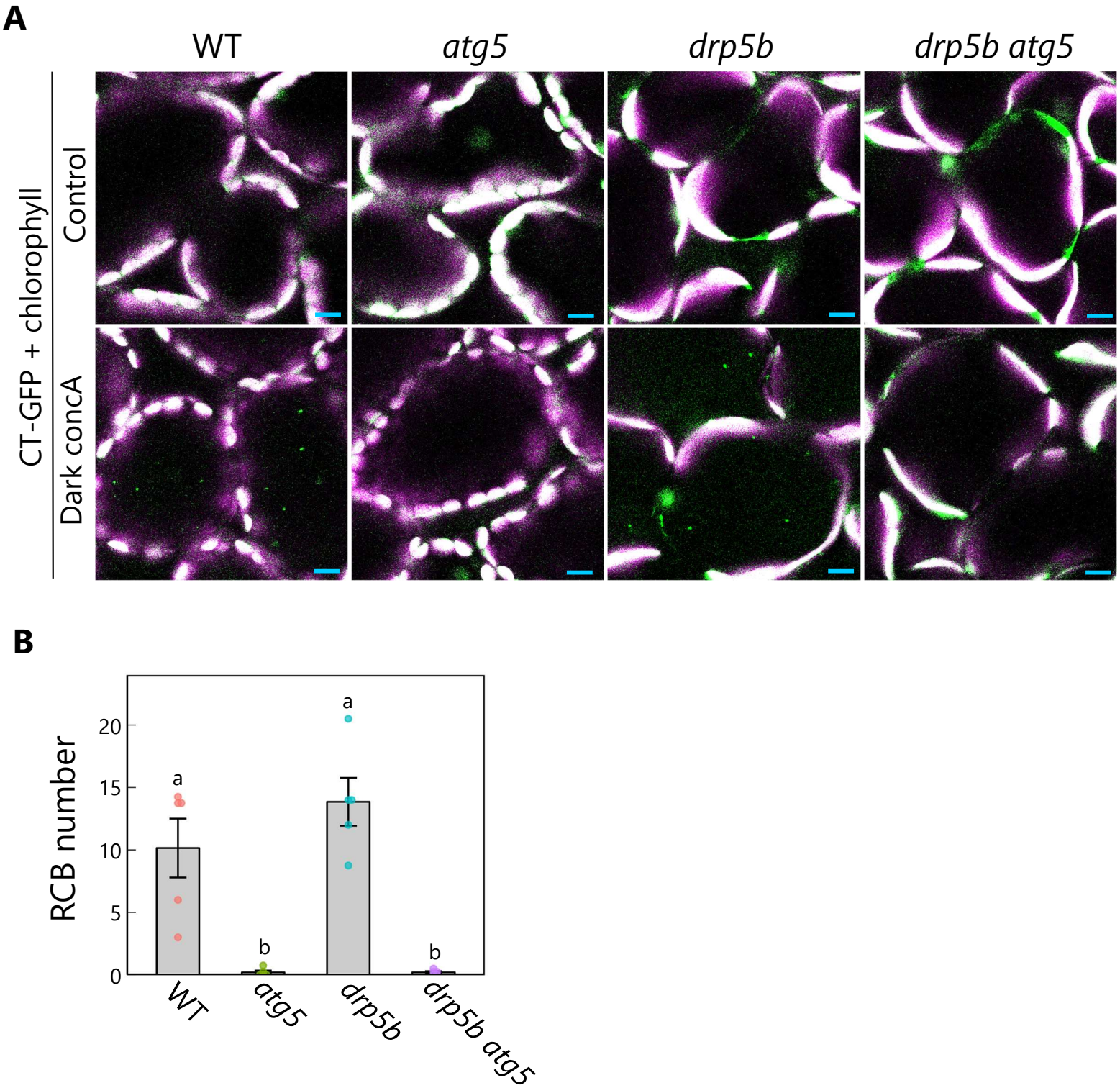

Figure 8–figure supplement 1. Production of Rubisco-containing bodies in *drp5b* mutants is ATG5-dependent.
(A) Confocal images of mesophyll cells from wild-type (WT), *atg5*, *drp5b*, and *drp5b atg5* leaves accumulating the stroma marker CT-GFP. Second rosette leaves were incubated in sugar-free solution containing 1 µM concanamycin A (concA) in darkness. Second rosette leaves from untreated plants were used as control. Green, CT-GFP; magenta, chlorophyll fluorescence. Only the merged channels are shown. Small vesicles containing CT-GFP without chlorophyll signal appear as green and are RCBs in the vacuole. Scale bars, 10 µm. (B) Number of accumulated RCBs, counted from the observations described in (A). Different lowercase letters denote significant differences based on Tukey's test ($P < 0.05$). Values are means ±SE ($n = 5$). Dots represent individual data points.

Figure 8–figure supplement 2

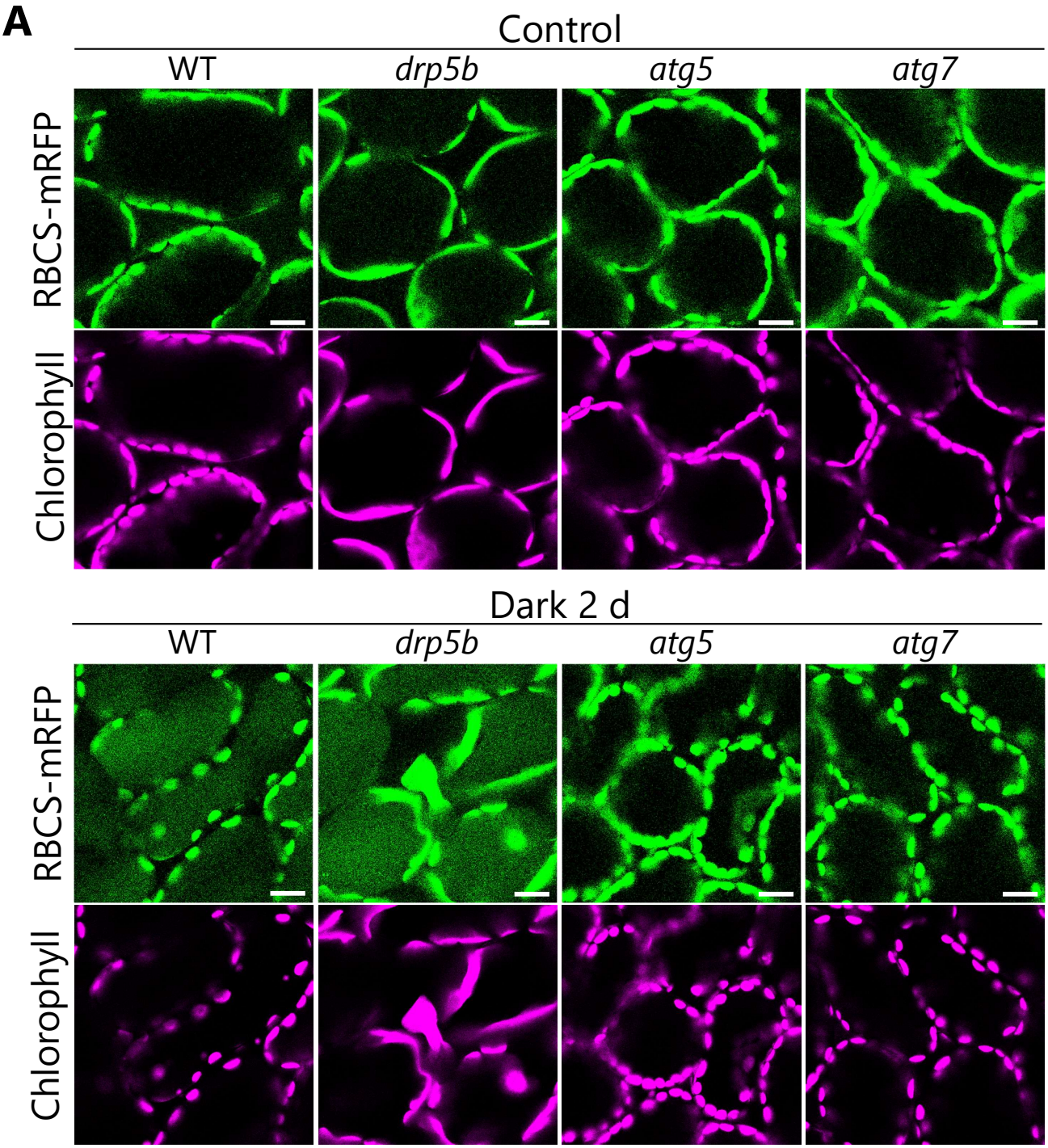

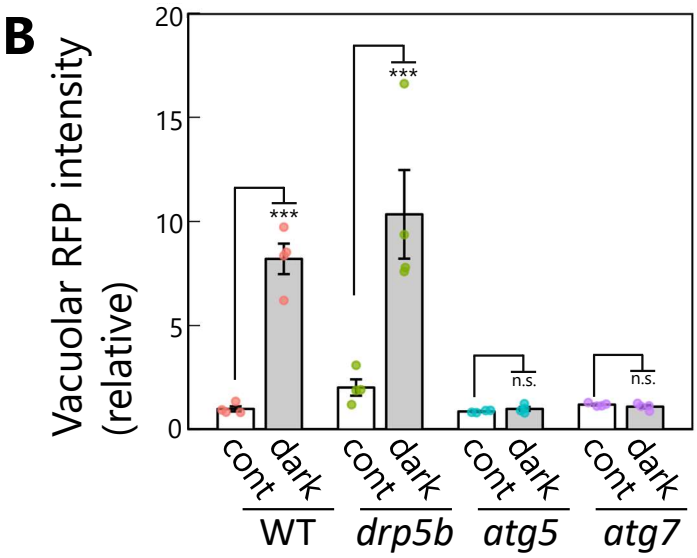

Figure 8–figure supplement 2. Vacuolar accumulation of stromal marker proteins in sugar-starved leaves.
(A) Confocal images of mesophyll cells from wild-type (WT), *drp5b*, *atg5*, and *atg7* leaves accumulating the stroma marker RBCS-mRFP. The leaves were incubated in sugar-free solution in darkness for 2 d. Second rosette leaves from untreated plants are shown as control. Green, RBCS-mRFP; magenta, chlorophyll fluorescence. Scale bars, 20 µm. (B) RFP intensity in the vacuolar lumen, as measured from the observations described in (A) and shown relative to that of untreated WT plants, which was set to 1. Asterisks denote significant differences based on *t*-test (***, $P < 0.05$; n.s., not significant). Values are means ± SE ($n = 4$). Dots represent individual data points.

detection of free mRFP derived from the vacuolar cleavage of RBCS-mRFP (Ono et al., 2013). When we incubated the leaves of plants accumulating RBCS-mRFP in darkness without concA, free mRFP levels increased in leaves of WT but not *atg5* or *atg7* plants (Figure 8C and 8D), indicating the occurrence of autophagy-dependent degradation of stromal proteins in response to sugar starvation in WT plants. The accumulation of free mRFP in the *drp5b* mutant was at least as high as that seen in WT plants (Figure 8C). The ratio of free mRFP to RBCS-mRFP increased in WT and *drp5b* plants after dark treatment (6.1 or 4.1 times higher in WT or *drp5b*, respectively), consistent with autophagy-mediated degradation of chloroplast fragments (Figure 8D). Confocal microscopy observations of mesophyll cells also showed the spread of mRFP signal in the vacuolar lumen in dark-treated leaves of WT and *drp5b* plants (Figure 8–figure supplement 2). These results indicate that the autophagic degradation of chloroplast stroma is active in both genotypes. The accumulation of free mRFP was 3.2 times higher in untreated leaves of *drp5b* compared with untreated WT leaves (Figure 8D); therefore, the activity of chloroplast autophagy might be constitutively higher in leaves of *drp5b* than in those of WT plants.

We directly observed the budding off of chloroplast fragments in leaves of the *drp5b* mutant. We incubated a leaf from the *drp5b* mutant accumulating RBCS-mRFP in darkness, which allowed us to observe the formation of a chloroplast bud and its release (Figure 9A, arrowheads; Video 13). In a leaf of the *drp5b* mutant accumulating RBCS-mRFP and GFP-ATG8a, we detected the vesiculation of a chloroplast fragment starting at the site to which the isolation membranes, labeled by GFP-ATG8a, were tightly associated (Figure 9B). The isolation membranes were anchored at two sites of a large chloroplast in a leaf of the *drp5b* mutant (Figure 9B, white and blue arrowheads); the chloroplast gradually protruded before releasing RCBs surrounded by autophagosomes (Figure 9B, Video 14). We conclude that DRP5B is dispensable for the autophagy-related division of chloroplast fragments.

Discussion

An unidentified machinery in piecemeal-type chloroplast autophagy

We previously demonstrated that chloroplast components in mesophyll cells are transported to the vacuole as a type of autophagic cargo termed RCBs to facilitate amino acid recycling (Ishida et al., 2008; Hirota et al., 2018). However, how a portion of chloroplasts is mobilized into the vacuolar lumen remained uncertain. In this study, high-resolution time-lapse imaging techniques allowed us to visualize the trafficking progression of chloroplast fragments from their parental chloroplasts to the vacuolar lumen. Importantly, we established that the development of the chloroplast-associated isolation membrane and the division of the chloroplast fragment occur simultaneously. This autophagy-related chloroplast division does not rely on DRP5B-mediated chloroplast division. Likewise, the formation of chloroplast buds is unlikely to be linked to the formation of stromules. Therefore, an unknown division machinery may be required for the autophagy-related division of chloroplast fragments. A similar organelle division mechanism takes place during mitophagy in mammals and budding yeast. The site of a mitochondrion that is associated with the isolation membrane protrudes and divides as the isolation membrane develops and becomes an enclosed autophagosome (Yamashita et al., 2016). This type of mitochondrial division is independent of Drp1 and Dnm1p. In yeast, the mitochondrial intermembrane-space protein mitofissin/Atg44 divides the mitochondrial fragment in coordination with autophagosome maturation (Fukuda et al., 2023). A functionally equivalent protein has not been identified in mammals.

Numerous studies have explored the molecular mechanisms of chloroplast division during the development of juvenile leaves (Chen et al., 2018). For instance, in Arabidopsis plants, ARC6 and PARALOG OF ARC6 (PARC6) mediate the tethering of the FTSZ ring on the chloroplast inner envelope (Vitha et al., 2003). PLASTID DIVISION 1 (PDV1) and PDV2 recruit DRP5B to the division site on the chloroplast outer envelope (Miyagishima et al., 2006). The ARC6–PDV2 and PARC6–PDV1 complexes may control the coordination of the stromal FTSZ

Fig. 9

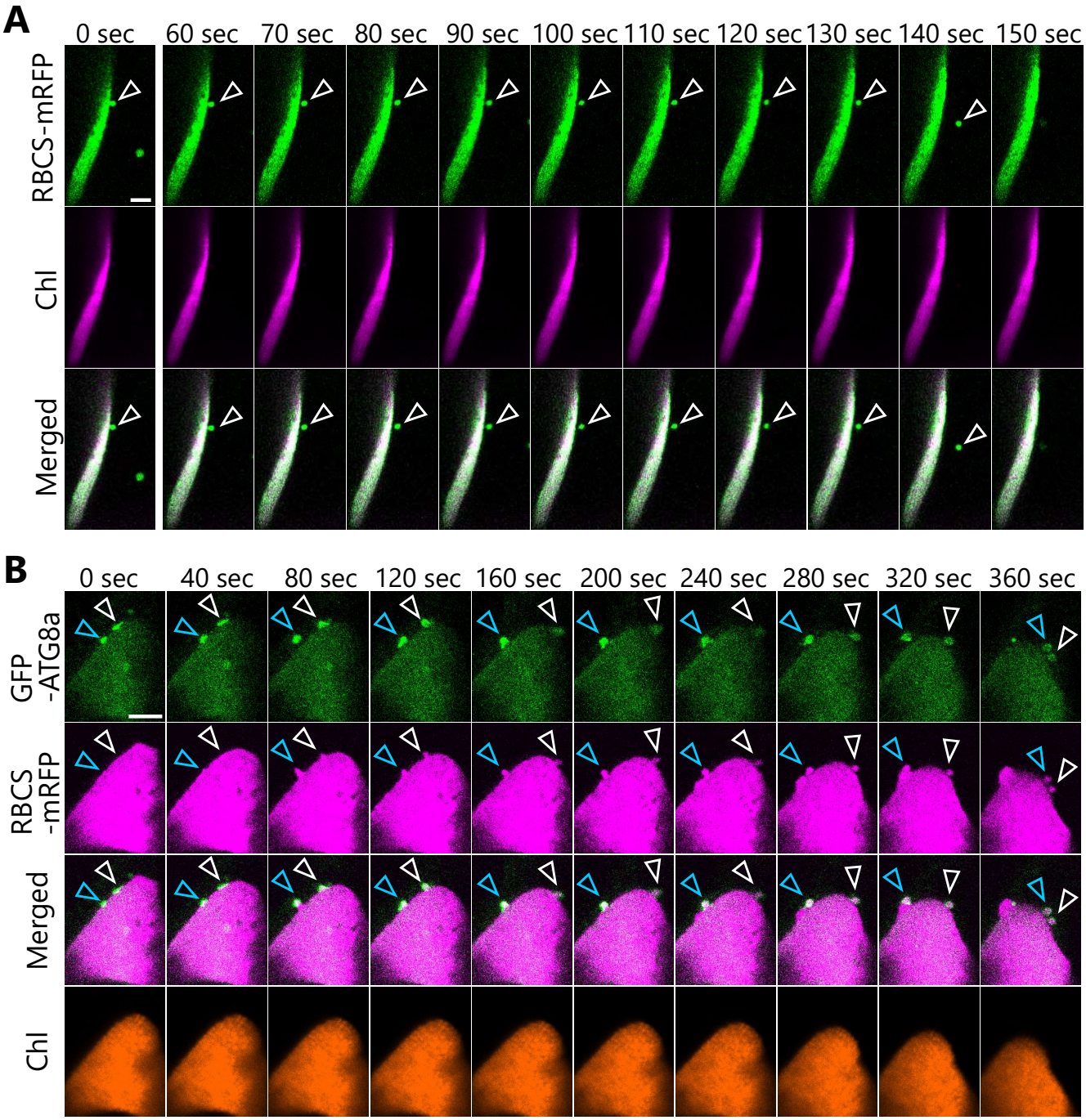

Figure 9. Formation and segmentation of chloroplast buds in leaves of the *drp5b* mutant.
(A) A leaf from the *drp5b* mutant accumulating the stroma marker RBCS-mRFP was incubated in sugar-free solution in darkness and then observed. Arrowheads indicate a chloroplast bud. Green, RBCS-mRFP; magenta, chlorophyll fluorescence (Chl). (B) A leaf from the *drp5b* mutant accumulating the stroma marker RBCS-mRFP and the isolation membrane marker GFP-ATG8a were incubated in sugar-free solution in darkness and then observed. Arrowheads indicate the position of the chloroplast-associated isolation membrane. White or blue arrowheads indicate different isolation-membrane-associated sites in a chloroplast, respectively. Green, GFP-ATG8a; magenta, RBCS-mRFP; orange, chlorophyll fluorescence (Chl). Scale bars, 5 µm.

ring and the cytosolic DRP5B ring (Wang et al., 2017; Chen et al., 2018). Therefore, the controlled division of plastids requires the cooperation of multiple protein complexes across the inner and outer envelopes. Nevertheless, whether chloroplasts divide during their piecemeal degradation has not been evaluated. It seems likely that autophagy-related division of chloroplast fragments needs to be carefully regulated, as the size of the segment has to fit into the autophagosome. Since the volume occupied by chloroplasts per cell is tightly regulated during cell expansion (Pyke and Leech, 1994), the decline of chloroplast volume during starvation or senescence might also be highly controlled. Further studies are needed to elucidate the molecular machinery underlying the autophagy-related division of chloroplast fragments for degradation.

Organelle-selective autophagy is typically controlled by receptor proteins that recognize the target organelles and act as a bridge between the organelles and isolation-membrane-anchored ATG8 (Farre and Subramani, 2016). The observation of a chloroplast-associated isolation membrane suggests that the receptors for chloroplast autophagy connect the isolation membrane to the chloroplast envelope. Such interaction might facilitate the development of the isolation membrane along the chloroplast surface. In budding yeast, the accumulation of the mitophagy receptor Atg32 is required for the formation of the mitophagosome. Atg32 binds to the mitochondrial outer membrane and interacts with Atg8 and Atg11, the latter being a scaffold protein recruiting other ATG members, for autophagosome formation. In fission yeast (*Schizosaccharomyces pombe*), Atg43 located on the mitochondrion outer membrane binds to Atg8 to stabilize the autophagosomal membrane for mitophagosome formation during starvation (Fukuda et al., 2020). In mammalian mitophagy, five types of mitophagy receptors have been identified that bind to LC3 (light chain 3) proteins, the mammalian orthologs of ATG8 (Onishi et al., 2021). Whether similar receptors work for chloroplast autophagy in mature leaves has not been established. Atg39 is the receptor for nucleophagy in budding yeast (Mochida et al., 2015), during which the condensation of Atg39 enables the protrusion of the nuclear membrane to be sequestered by the autophagosome (Mochida et al., 2022). The accumulation of receptor proteins might contribute to the morphological changes required for chloroplasts to form RCBs.

Roles of stromules

The molecular functions of stromules are not completely understood. We first predicted a functional link between stromules and RCBs such that stromules are vesiculated and become RCBs for autophagic degradation. However, our imaging assays revealed that chloroplast stromule formation is not essential for RCB formation in mesophyll cells (Figure 6). The use of the *sid2* mutant and NahG transgenic lines indicated the close association between enhanced SA signaling and the elevated stromule formation observed in *atg* mutants (Figure 7). This finding is consistent with the suggested role of stromules in inducing programmed cell death as an SA-dependent immune response (Caplan et al., 2015). We assign the enhanced stromule formation in *atg* mutant leaves as a consequence of their higher SA and ROS levels, alone or in combination with the excess stromal fraction accumulating in these mutants due to impaired RCB formation.

In root cells, an association of the isolation membrane with stromules of non-green plastids was reported (Spitzer et al., 2015). Stromule formation is more common in the non-green plastids of tissues without photosynthetic activity than in the mature chloroplasts in leaf mesophyll cells (Hanson and Sattarzadeh, 2008). Therefore, the interaction between stromules and the isolation membrane might be important for the efficient degradation of non-green plastids by autophagy. Our study focused on the degradation mechanism of mature chloroplasts in leaves, since mature chloroplasts are rich in nutrients and amino acids and their degradation is particularly important for plant nutrient recycling (Makino and Osmond, 1991). There might also be differences in the degradation mechanism of plastids among cell types.

Intracellular dynamics for the transport of RCBs

Soluble *N*-ethylmaleimide-sensitive factor attachment protein receptors (SNAREs) mediate

versatile membrane fusion events (Ito and Uemura, 2022). Multiple SNARE proteins participate in the fusion of the lysosomal/vacuolar membrane to the autophagosomal membrane in mammals and budding yeast. A recent study reported the involvement of the Arabidopsis SNARE proteins, VESICLE-ASSOCIATED MEMBRANE PROTEIN 724 (VAMP724) and VAMP726, in autophagosome formation (He et al., 2022). In this study, we observed an interesting morphology of vacuolar membranes that incorporate RCBs into the vacuole (Figure 4). A similar phenomenon was previously observed during the transport of pexophagosomes (autophagosomes containing peroxisome components) in Arabidopsis leaves (Oikawa et al., 2022). Thus, the transient engulfment of an autophagosome by the vacuolar membrane might be a common phenomenon for vacuolar incorporation in leaf mesophyll cells. In mammals, two autophagosomal membrane-anchored SNAREs, Syntaxin 17 (Stx17) and Ykt6, independently contribute to the autophagosome-lysosome fusion (Itakura et al., 2012; Matsui et al., 2018). Stx17 translocates to the closed autophagosome transiently, enabling its fusion with the lysosome (Tsuboyama et al., 2016). Such a translocation system might allow the recruitment of the vacuolar membrane for its fusion with the mature autophagosomes in plant cells.

The current study revealed how a type of piecemeal autophagy transports chloroplast stroma and envelope components into the vacuole for degradation in mature Arabidopsis leaves. The key event is the development of the isolation membrane along the chloroplast surface, which might lead to the protrusion and segmentation of the membrane-contact site of a chloroplast. Proteins mediating chloroplast segmentation and the interaction between the chloroplast surface and the isolation membrane remain to be uncovered. This study developed a live-cell tracking method for piecemeal-type chloroplast autophagy, which will help future studies elucidate the underlying mechanisms of the intracellular dynamics of this type of autophagy.

Materials and Methods

Plant materials

Arabidopsis (*Arabidopsis thaliana*) plants from the Columbia accession (Col) were used in this study. Plants were grown in soil in growth chambers at 23°C under a 12-h light/12-h dark photoperiod with illumination from fluorescent lamps or LEDs (90–130 μmol m^{-2} s^{-1}). The T-DNA-insertion mutants for *ATG5* (*atg5-1*; SAIL_129_B07), *ATG7* (*atg7-2*; GABI_655B06), *ATG2* (*atg2-1*; SALK_076727), *ATG10* (*atg10-1*; SALK_084434), and *DRP5B* (*arc5-2*; SAIL_71_D11) have been described previously (Doelling et al., 2002; Thompson et al., 2005; Miyagishima et al., 2006; Phillips et al., 2008; Yoshimoto et al., 2009). The *sid2-2* mutant and a transgenic line expressing NahG have been reported previously (Delaney et al., 1994; Yoshimoto et al., 2009). The transgenic plants expressing a construct encoding chloroplast stroma-targeted GFP under the control of the cauliflower mosaic virus (CaMV) 35S promoter (*Pro35S:CT-GFP*), chloroplast stroma-targeted DsRed from the CaMV 35S promoter (*Pro35S:CT-DsRed*), RBCS2B-GFP from the Arabidopsis *RBCS2B* promoter (*ProRBCS:RBCS-GFP*), VHP1-mGFP from the Arabidopsis *VHP1* promoter (*ProVHP1:VHP1-mGFP*), GFP-ATG8a from the Arabidopsis *UBQ10* promoter (*ProUBQ:GFP-ATG8a*), and TOC64-mRFP from the Arabidopsis *TOC64* promoter (*ProTOC64:TOC64-mRFP*) have been reported in previous studies (Kohler et al., 1997; Ishida et al., 2008; Segami et al., 2014; Ishida et al., 2021; Nakamura et al., 2021b; Kusano et al., 2023). Transgenic plants expressing *RBCS2B-EYFP*, *RBCS2B-mRFP*, or *RBCS2B-tagRFP* from the *RBCS2B* promoter (*ProRBCS:RBCS-EYFP*, *ProRBCS:RBCS-mRFP*, *ProRBCS:RBCS-tagRFP*) were generated as follows. A genomic fragment encompassing the promoter region and the full-length coding region of *RBCS2B* (At5g38420), cloned into the pENTR/D/TOPO vector (Ishida et al., 2008), was inserted into the Gateway vectors pGWB540, pGWB553, or pGWB559 (Nakagawa et al., 2007) via LR clonase (Invitrogen) reaction to generate constructs encoding RBCS2B-EYFP, RBCS2B-mRFP, or RBCS2B-tagRFP, respectively.

Transgenic plants expressing *ATPC1-tagRFP* (*ProATPC1:ATPC1-tagRFP*) were

produced as follows. A genomic fragment containing the promotor region and full-length coding region of *ATPC1* (At4g04640) was amplified from Col-0 genomic DNA by PCR using PrimeSTAR DNA polymerase (TaKaRa) and the primers ATPC1_F (CACCCATGGAGAGGGCTCGTACCTTAC) and ATPC1_R (AACCTGTGCATTAGCTCCAG), cloned into pENTR/D-TOPO (Invitrogen), and then recombined into the vector pGWB559 via LR reaction. The resulting construct was introduced into Arabidopsis plants by the floral dip method (Clough and Bent, 1998) using Agrobacterium (*Agrobacterium tumefaciens*) strain GV3101. Transgenic plants expressing two types of fluorescent markers and mutant plants expressing fluorescent markers were generated by crossing or additional transformations.

Live-cell imaging by confocal microscopy

The second rosette leaves of 20- to 24-d-old plants were used for time-lapse imaging of living cells. The leaves were excised, infiltrated with sugar-free solutions, and incubated in darkness for 5 to 24 h, followed by confocal microscopy observations. When the dark treatment was started at the end of the night, the incubation time was around 5–9 h. When the treatment was started during the light period, the incubation time was around 20–24 h. The sugar-free solutions contained 10 mM MES-NaOH, pH 5.5, alone or with full-strength Murashige and Skoog salts (Shiotani M. S.) or the photosynthesis inhibitor 3-(3,4-dichlorophenyl)-1,1-dimethylurea (DCMU).

Time-lapse imaging in Figure 1 was performed as previously described with a two-photon excitation confocal microscope with a spinning-disk unit (Otomo et al. 2015). The GFP signal was excited by 920-nm femtosecond light pulses generated by a mode-locked titanium-sapphire laser light source (Mai Tai eHP DeepSee; Spectra Physics). The YFP, RFP, and chlorophyll signals were excited by 1040-nm femtosecond light pulses generated by an ytterbium laser light source (femtoTrain; Spectra Physics). The fluorescent signals were observed under an inverted microscope (IX-71; Olympus) equipped with a spinning-disk scanner with 100-μm-wide pinholes aligned with a Nipkow disk (CSU-MPϕ100; Yokogawa Electric) and a water-immersion lens (UPLSAPO60XW, numerical aperture [NA] = 1.20, Olympus). The fluorescence images were captured by an EM-CCD camera (EM-C2; Qimaging or iXon Ultra 897; Andor Technology) through a bandpass filter for GFP and YFP (BrightLine 528/38; Semrock), RFP (D630/60M; Chroma Technology), or chlorophyll autofluorescence (BrightLine 685/40; Semrock). For the simultaneous detection of YFP and chlorophyll signals, fluorescence was detected through image-splitting optics (W-View Gemini; Hamamatsu Photonics) including a dichroic mirror (FF580-FDi01-25 36; Semrock) and the bandpass filters. Z-Scans were performed with a piezo actuator (P-721; PI). The acquired images were processed and analyzed using NIS-Elements C software (Nikon) or Imaris software (Bitplane).

Time-lapse imaging analysis by confocal laser-scanning microscopy was performed with LSM800 (Carl Zeiss), LSM880 (Carl Zeiss), LSM900 (Carl Zeiss), or SP8 (Leica) systems. A water-immersion objective lens (LD C-Apochromat 63x, NA = 1.15; Carl Zeiss) or an oil-immersion objective lens (HC PL APO 63x, NA = 1.40, Leica) was used. Fast Airyscan mode was used for the observation displayed in Figure 4B with the LSM880 system.

Quantification of microscopy images

Confocal images used for the quantification of RCB numbers (Figure 1–figure supplement 1, Figure 5, Figure 8), chloroplast protrusions (Figure 5), stromules (Figure 7), or vacuolar RFP intensity (Figure 8–figure supplement 2) were acquired with a C2 system (Nikon) equipped with a water-immersion objective lens (CFI Apochromat LWD Lambda S 40XC, NA = 1.2; Nikon). RFP emission was detected at 580–630 nm (bandpass filter RPB580–630; Omega optical) after excitation with a 559.8-nm diode laser; chlorophyll autofluorescence was detected at 660–720 nm following excitation by a 636.5-nm diode laser; the two signals were detected simultaneously. For the simultaneous detection of GFP and chlorophyll, GFP emission was detected at 500–550 nm

(bandpass filter RPB500–550; Omega Optical) following excitation by a 489.6-nm diode laser; chlorophyll autofluorescence was detected at 660–720 nm following excitation by a 489.6-nm diode laser.

For the quantification of RCBs and chloroplast protrusions, the second rosette leaves of 21-d-old plants were excised and incubated in 10 mM MES-NaOH, pH 5.5, containing 1 μM concanamycin A (Santa Cruz) for 1 d in darkness at 23°C. The stock solution was 100 μM concanamycin A in DMSO. Sucrose (1%, w/v) or full-strength MS salts was added as energy source or nutrients, respectively. The number of accumulated RCBs in a fixed area (215.04 × 215. 04 μm each) was counted. The mean number from four areas of one second rosette leaf per plant was calculated from four or five independent plants. The *z*-stack images of the 3D region (215.04 × 215.04 × 15 μm each) were observed, and the proportion of chloroplasts forming protrusions out of 50 chloroplasts was scored in the region. The mean from two different regions of one second rosette leaf per plant was calculated from four independent plants.

Chloroplast stromule formation in guard cells was observed in the second rosette leaves of 13-d-old seedlings. The proportion of chloroplasts forming stromules in each pair of guard cells was scored from the *z*-stack images (251.04 × 251.04 × 20 μm each). The mean from 10 stomata of one second rosette leaf per plant was calculated from three individual seedlings. Chloroplast stromule formation in mesophyll cells was observed in the third rosette leaves of 20-d-old or 36-d-old plants. The proportion of chloroplasts forming stromules out of 50 chloroplasts was scored in the *z*-stack images (215.04 × 215.04 × 15 μm each). The mean from two different regions of one third rosette leaf per plant was calculated from four individual plants.

For the quantification of vacuolar RFP intensity, the second rosette leaves of 21-d-old plants were excised and incubated in 10 mM MES-NaOH, pH 5.5, for 2 d in darkness at 23°C. The RFP intensity in the central area of a mesophyll cell (15.2 × 15.2 μm each) was measured. The mean from 12 cells of one second rosette leaf per plant was calculated from four individual plants.

Protein analysis

The second and third rosette leaves of 21-d-old plants were incubated in darkness in 10 mM MES-NaOH, pH 5.5, for 2 d and then frozen in liquid nitrogen. The leaves from 23-d-old, untreated plants were used as control. The frozen leaves were homogenized using a tissue laser (Qiagen) and a zirconium bead, before being resuspended in homogenization buffer containing 50 mM HEPES-NaOH pH 7.5, 16 mM DTT, 10% (v/v) glycerol, and protease inhibitor cocktail (Nacalai). Following centrifugation at 20,630 *g* for 10 min at 4°C, the protein amounts in the supernatants were measured using a 660-nm Protein Assay Reagent (Pierce). The supernatants were then mixed with an equal volume of SDS sample buffer containing 200 mM Tris-HCl pH 8.5, 20% (v/v) glycerol, 2% (w/v) SDS and 0.1 M DTT, and incubated for 5 min at 95°C. An equal amount of protein was subjected to SDS-PAGE using TGX FastCast acrylamide gels (Bio-Rad) and transfer to nitrocellulose membrane (Trans-blot turbo transfer pack; Bio-Rad). An anti-RFP 1G9 clone antibody (1:2000, M204-3; MBL) and an anti-cFBPase antibody (1:5000, AS04043; Agrisera) were used as primary antibodies. Goat anti-mouse IgG (H+L) secondary antibody DyLight 800 4X PEG (1:10000, SA5-35571; Invitrogen) or goat anti-rabbit HRP secondary antibody (1:10000, NA931; Cytiba) was used as secondary antibody for RFP or cFBPase detection, respectively. The chemiluminescence signals developed with SuperSignal West Dura Extended Duration Substrate (Pierce) and the DyLight 800 fluorescent signals were detected by a ChemiDoc MP system (Bio-Rad). The image processing and the quantification of band intensity were performed using Image Lab Software (Bio-Rad).

Hydrogen peroxide measurements

The amount of H_2O_2 in leaf lysates was measured as previously described (Chakraborty et al., 2016) with an Amplex Red Hydrogen Peroxide/Peroxidase Assay Kit (Invitrogen) and an Infinite

200 PRO plate reader (Tecan).

Statistical analysis

Statistical analysis in this study was performed with JMP14.3.0 software (SAS Institute). Student's t test or Tukey's test was used to compare paired samples or multiple samples, respectively.

Acknowledgements

We thank Emi Sone, Izumi Fukuhara, and Mio Tokuda for their technical support. We thank Dr. Kohki Yoshimoto for the use of *atg*, *sid2*, and NahG plants, Dr. Maureen R. Hanson for the use of *Pro35S:CT-GFP* plants, Dr. Shoji Segami for the use of the *ProVHP1:VHP1-mGFP* construct, and Dr. Tsuyoshi Nakagawa for the use of pGWB vectors.

Figure legends

Figure 1. Chloroplast buds are released in sugar-starved leaves.

Time-lapse observations of 3D-reconstructed chloroplast morphology in Arabidopsis mesophyll cells accumulating chloroplast stroma-targeted fluorescent markers. A leaf from a plant accumulating chloroplast stroma-targeted GFP (CT-GFP) (A), RBCS-mRFP (B), or RBCS-EYFP (C) was incubated in sugar-free solution in darkness and then observed through a two-photon excitation microscope equipped with a confocal spinning disk unit. Images in (A–C) are still frames from videos 1, 2, and 3, respectively. Arrowheads indicate chloroplast budding structures. Scale bars, 5 µm. In (C), green, RBCS-EYFP; magenta, chlorophyll fluorescence. In the merged images, the overlapping regions of RBCS-EYFP and chlorophyll signals appear white.

Figure 1–figure supplement 1. Accumulation of chloroplast stroma components in the vacuole via autophagy.

Confocal images of mesophyll cells from wild-type (A) or *atg7* (B) plants accumulating the chloroplast stroma marker RBCS-mRFP. The excised leaves were incubated in 10 mM MES-NaOH containing 1 µM concanamycin A (concA) in darkness. Sucrose (Suc) or Murashige and Skoog salts (MS) were added as an energy or nutrient source, respectively. Second rosette leaves from nontreated plants are shown as control. Green, RBCS-mRFP; magenta, chlorophyll fluorescence. Scale bars, 10 µm. The small vesicles containing RBCS-mRFP without chlorophyll signal appear as green and are Rubisco-containing bodies (RCBs) in the vacuole. (C) Number of accumulated RCBs from the observations described in (A) and (B). Different lowercase letters denote significant differences based on Tukey's test ($P < 0.05$). Values are means ±SE ($n = 4$). Dots represent individual data points.

Video 1. Release of a chloroplast bud as visualized by chloroplast-targeted GFP.

A leaf accumulating the chloroplast stroma-targeted GFP (CT-GFP) was incubated in sugar-free solution in darkness for time-lapse imaging with a two-photon excitation microscope equipped with a confocal spinning-disk unit. 3D-reconstructed images (8 µm in depth) acquired about every 3 sec are displayed at 10 frames/sec. Scale bar, 5 µm. This video was used to generate Figure 1A.

Video 2. Release of a chloroplast bud as visualized by RBCS-mRFP

A leaf accumulating the chloroplast stroma marker RBCS-mRFP was incubated in sugar-free solution in darkness for time-lapse imaging with a two-photon excitation microscope equipped with a confocal spinning-disk unit. 3D-reconstructed images (2 µm in depth) acquired about every 1.2 sec are displayed at 10 frames/sec. Scale bar, 5 µm. This video was used to generate Figure 1B.

Video 3. Tracking of the stroma marker and chlorophyll fluorescence during the release of a chloroplast bud.
A leaf accumulating the chloroplast stroma marker RBCS-EYFP was incubated in sugar-free solution in darkness for time-lapse imaging with a two-photon excitation microscope equipped with a confocal spinning-disk unit. 3D-reconstructed images (8 µm in depth) acquired every 4 sec are displayed at 10 frames/sec. Scale bar, 5 µm. Green, RBCS-EYFP; magenta, chlorophyll fluorescence. Only the video of the merged channels is shown. The overlapping regions of RBCS-EYFP and chlorophyll signals appear white. This video was used to generate Figure 1C.

Figure 2. Chloroplast buds containing stroma and envelope components are released from the chloroplasts.
Time-lapse observations of Arabidopsis mesophyll cells accumulating the chloroplast stroma marker along with an envelope marker or a thylakoid membrane marker. Leaves accumulating stromal RBCS-GFP along with envelope-bound TOC64-mRFP (A and B) or with thylakoid membrane-bound ATPC1-tagRFP (C and D) were incubated in sugar-free solution in darkness and then observed. Images in (B) or (D) are still frames from Videos 4 and 5, respectively. Arrowheads indicate chloroplast budding structures. Scale bars, 5 µm. Green, TOC64-mRFP or ATPC1-tagRFP; magenta, RBCS-GFP; orange, chlorophyll (Chl) fluorescence. The graphs in (A and C) show fluorescence intensities along the blue lines (a to b) in the magnified images of the area indicated by dashed blue boxes. The intensities are shown relative to the maximum intensity for each fluorescence channel, set to 1.

Video 4. A released chloroplast bud contains the envelope marker TOC64-mRFP.
A leaf accumulating the chloroplast stroma marker RBCS-GFP and the envelope marker TOC64-mRFP was incubated in sugar-free solution in darkness for time-lapse imaging. Images acquired every 2 sec are displayed at 10 frames/sec. Scale bar, 5 µm. Green, TOC64-mRFP; magenta, RBCS-GFP. Only the video of the merged channels is shown. This video was used to generate Figure 2B.

Video 5. A released chloroplast bud does not contain the thylakoid membrane marker ATPC1-tagRFP.
A leaf accumulating the chloroplast stroma marker RBCS-GFP and the thylakoid membrane marker ATPC1-tagRFP was incubated in sugar-free solution in darkness for time-lapse imaging. Images acquired every 2 sec are displayed at 10 frames/sec. Scale bar, 5 µm. Green, ATPC1-tagRFP; magenta, RBCS-GFP. Only the video of the merged channels is shown. This video was used to generate Figure 2D.

Figure 3. Tracking the transport of a Rubisco-containing body.
A leaf accumulating chloroplast-stroma targeted GFP (CT-GFP) was incubated in sugar-free solution in darkness and the transport of a Rubisco-containing body (RCB) was tracked. (A) Confocal images during the periods when the RCB moved quickly (24.4–34.8 and 73.8–90.5 sec). Arrowheads indicate an RCB. The images were generated from Video 6. Green, CT-GFP; magenta, chlorophyll (Chl) fluorescence. In the merged images, the overlapping regions of RBCS-GFP and chlorophyll signals appear white. Scale bar, 5 µm. (B) Calculated speed of the tracked RCB in (A). (C) The track of the RCB. The color of the track line changes over time, as indicated by the color bar. Scale bar, 2 µm.

Video 6. Tracking of a Rubisco-containing body.
A leaf accumulating chloroplast-stroma targeted GFP (CT-GFP) was incubated in sugar-free solution in darkness for time-lapse imaging monitoring of an RCB marked by CT-GFP. Images acquired every 0.52 sec are displayed at 20 frames/sec. Scale bar, 5 µm. Green, CT-GFP; magenta,

chlorophyll fluorescence. Only the video of the merged channels is shown. This video was used to generate Figure 3A.

Figure 4. Dynamics of the vacuolar membrane during the incorporation of Rubisco-containing bodies.
Leaves accumulating the chloroplast stroma marker RBCS-mRFP along with the vacuolar membrane marker VHP1-mGFP were incubated in sugar-free solution in darkness and the behavior of cytosolic RCBs was monitored. The images when the vacuolar membrane engulfs an RCB (25.4–30.5 sec in A and 52.6–57.4 sec in B) and when an RCB is incorporated into the vacuolar lumen (47.0–52.0 sec in A and 65.3–72.9 in B) are shown. The images in (A) and (B) are still frames from Videos 7 and 8, respectively. Open arrowheads indicate an RCB engulfed by the vacuolar membrane. Closed arrowheads indicate the open site of the vacuolar membrane for the incorporation of an RCB. V indicates the region of the vacuolar lumen. Green, VHP1-mGFP; magenta, RBCS-mRFP. Scale bars, 5 µm.

Video 7. Incorporation of a Rubisco-containing body into the vacuolar lumen.
A leaf accumulating the chloroplast stroma marker RBCS-mRFP along with the vacuolar membrane marker VHP1-mGFP was incubated in sugar-free solution in darkness for time-lapse imaging. Images acquired every 1.27 sec are displayed at 10 frames/sec. Scale bar, 5 µm. Green, VHP1-mGFP; magenta, RBCS-mRFP. Only the video of the merged channels is shown. This video was used to generate Figure 4A.

Video 8. Another video for the vacuolar incorporation of a Rubisco-containing body.
A leaf accumulating the chloroplast stroma marker RBCS-mRFP along with the vacuolar membrane marker VHP1-mGFP was incubated in sugar-free solution in darkness for time-lapse imaging. Images acquired every 0.317 sec are displayed at 25 frames/sec. Scale bar, 5 µm. Green, VHP1-mGFP; magenta, RBCS-mRFP. Only the video of the merged channels is shown. This video was used to generate Figure 4B.

Figure 5. Autophagy deficiency does not increase the number of chloroplast protrusions during a 1-d dark treatment.
Leaves from wild-type (WT), *atg5*, or *atg7* plants accumulating the chloroplast stroma marker RBCS-mRFP were incubated in sugar-free solution containing 1 µM concanamycin A (concA) for 1 d in darkness. 2D images of mesophyll cells were acquired (A), and the number of accumulated RCBs in the vacuoles was scored (B). Leaves from untreated plants are shown as control. The appearance of chloroplast protrusions was observed from orthogonal projections created from *z*-stack images (15 µm in depth; C), and the proportion of chloroplasts having protrusion structures was calculated (D). Scale bars, 10 µm. Green, RBCS-mRFP; magenta, chlorophyll fluorescence. Only the merged channels are shown. The overlapping regions of RBCS-mRFP and chlorophyll signals appear white. Small vesicles containing RBCS-mRFP without chlorophyll signal appear as green and are RCBs in the vacuole. Arrowheads indicate the structures that were counted as a chloroplast protrusion in (D). Different lowercase letters denote significant differences based on Tukey's test ($P < 0.05$). Values are means ±SE ($n = 4$). Dots represent individual data points in each graph.

Figure 5–figure supplement 1. Chloroplast protrusions do not increase in *atg2* or *atg10* mutant leaves during a 1-d dark treatment.
The experiments described in Figure 5 were performed on leaves from wild-type (WT), *atg2*, or *atg10* plants accumulating the chloroplast stroma marker RBCS-mRFP. Scale bars, 10 µm. Green, RBCS-mRFP; magenta, chlorophyll fluorescence. Only the merged channels are shown. The overlapping regions of RBCS-mRFP and chlorophyll signals appear white. Small vesicles

containing RBCS-mRFP without chlorophyll signal appear as green and are RCBs in the vacuole. Arrowheads indicate the structures that were counted as a chloroplast protrusion in (D). Different lowercase letters denote significant differences based on Tukey's test ($P < 0.05$). Values are means ±SE ($n = 4$). Dots represent individual data points in each graph.

Figure 6. The formation of a chloroplast bud and the maturation of the chloroplast-associated isolation membrane occur concomitantly.
Leaves accumulating the chloroplast stroma marker, RBCS-mRFP (A) or CT-DsRed (B), and the isolation membrane marker GFP-ATG8a were incubated in sugar-free solution in darkness and then observed. Arrowheads indicate the position of the chloroplast-associated isolation membrane. Images in (A) and (B) are still frames from Videos 9 and 10, respectively. Green, GFP-ATG8a; magenta, RBCS-mRFP or CT-DsRed. Scale bars, 5 µm. (C) Time-dependent changes in the ratio of the major axis to the minor axis in the GFP-ATG8a-labeled isolation membrane (top), or in the area of the chloroplast protrusion (bottom) as measured from the images in (B).

Video 9. Protrusion of the isolation-membrane-associated site within a chloroplast.
A leaf accumulating the chloroplast stroma marker RBCS-mRFP and the isolation membrane marker GFP-ATG8a were incubated in sugar-free solution in darkness for time-lapse imaging. Images acquired every 4.0 sec are displayed at 10 frames/sec. Scale bar, 5 µm. Green, GFP-ATG8a; magenta, RBCS-mRFP. Only the video of the merged channels is shown. This video was used to generate Figure 6A.

Video 10. Autophagosome development and chloroplast segmentation occur concomitantly.
A leaf accumulating the chloroplast stroma-targeted DsRed (CT-DsRed) and the isolation membrane marker GFP-ATG8a were incubated in sugar-free solution in darkness for time-lapse imaging. Images acquired every 1.0 sec are displayed at 20 frames/sec. Scale bar, 5 µm. Green, GFP-ATG8a; magenta, CT-DsRed. Only the video of the merged channels is shown. This video was used to generate Figure 6B.

Figure 6–figure supplement 1. Another observation of the protrusion of the isolation-membrane-associated site in a chloroplast.
A leaf accumulating the chloroplast stroma marker CT-DsRed and the isolation membrane marker GFP-ATG8a was incubated in sugar-free solution in darkness and then observed. Arrowheads indicate the position of the chloroplast-associated isolation membrane. The images are still frames from Video 11. Green, GFP-ATG8a; magenta, CT-DsRed. Scale bars, 5 µm. (B) Time-dependent changes in the ratio of the major axis to the minor axis in the GFP-ATG8a-labeled isolation membrane (top), or in the area of the chloroplast protrusion (bottom), as measured from the images in (A).

Figure 6–figure supplement 2. Chloroplast buds surrounded by the isolation membrane appear in multiple chloroplasts.
A leaf accumulating the chloroplast stroma marker RBCS-tagRFP and the isolation membrane marker GFP-ATG8a were incubated in sugar-free solution in darkness and then observed. White, yellow, or blue arrowheads indicate the isolation-membrane-associated site in different chloroplasts, respectively. The images are still frames from Video 12. Green, GFP-ATG8a; magenta, RBCS-tagRFP; orange, chlorophyll (Chl) fluorescence. Scale bars, 5 µm.

Video 11. Another time-lapse assay showing the concomitant progression of autophagosome development and chloroplast segmentation.
A leaf accumulating the chloroplast stroma-targeted DsRed (CT-DsRed) and the isolation membrane marker GFP-ATG8a were incubated in sugar-free solution in darkness for time-lapse

imaging. Images acquired every 2.0 sec are displayed at 10 frames/sec. Scale bar, 5 µm. Green, GFP-ATG8a; magenta, CT-DsRed. Only the video of the merged channels is shown. This video was used to generate Figure 6B.

Video 12. Autophagy-related chloroplast segmentation occurs in sequence.
A leaf accumulating the chloroplast stroma marker RBCS-tagRFP and the isolation membrane marker GFP-ATG8a were incubated in sugar-free solution in darkness for time-lapse imaging. Images acquired every 2.0 sec are displayed at 10 frames/sec. Scale bar, 5 µm. Green, GFP-ATG8a; magenta, RBCS-tagRFP. Only the video of the merged channels is shown. This video was used to generate Figure 6A.

Figure 7. Diminished salicylic acid signal suppresses stromule formation in autophagy-deficient mutants.
(A) Confocal images of guard cells from wild-type (WT), *atg5*, NahG, and *atg5* NahG leaves accumulating chloroplast stroma-targeted GFP (CT-GFP). Scale bars, 10 µm. (B) Percentage of chloroplasts forming stromules, from the observations described in (A). (C) Confocal images of guard cells from WT, *atg5*, *atg7*, *sid2*, *sid2 atg5*, and *sid2 atg7* leaves accumulating CT-GFP. Scale bars, 10 µm. (D) Percentage of chloroplasts forming stromules, from the observations described in (C). In (A) and (C), orthogonal projections produced from *z*-stack images (10 µm in depth) are shown. (E) Orthogonal projections produced from *z*-stack images (15 µm in depth) of mesophyll cells from WT, *atg5*, *atg7*, *sid2*, *sid2 atg5*, and *sid2 atg7* leaves accumulating CT-GFP. Third rosette leaves from 36-d-old plants were observed. Green, CT-GFP; magenta, chlorophyll fluorescence. Only the merged channels are shown. Scale bars, 20 µm. (F) Percentage of chloroplasts forming stromules in mesophyll cells, from the observations described in (E). (G) Hydrogen peroxide (H_2O_2) content in WT, *atg5*, *atg7*, *sid2*, *sid2 atg5*, and *sid2 atg7* leaves. Different lowercase letters denote significant differences based on Tukey's test ($P < 0.05$). Values are means ±SE ($n = 3$ in B and D or 4 in F and G). Dots represent individual data points in each graph.

Figure 7–figure supplement 1. Autophagy deficiency does not activate stromule formation from mesophyll chloroplasts in young leaves.
Orthogonal projections produced from *z*-stack images (15 µm in depth) of mesophyll cells from WT, *atg5*, *atg7*, *sid2*, *sid2 atg5*, and *sid2 atg7* leaves accumulating CT-GFP. The third rosette leaves from 20-d-old plants were observed. Green, CT-GFP; magenta, chlorophyll fluorescence. Only the merged channels are shown. Scale bars, 20 µm.

Figure 8. DRP5b is dispensable for chloroplast autophagy in sugar-starved leaves.
Confocal images of mesophyll cells from wild-type (WT) and *drp5b* leaves accumulating the stroma marker RBCS-mRFP. Second rosette leaves were incubated in sugar-free solution containing 1 µM concanamycin A (concA) in darkness. Green, RBCS-mRFP; magenta, chlorophyll fluorescence. Scale bars, 10 µm. (B) Number of accumulated RCBs in WT, *drp5b*, *atg5*, and *atg7* leaves, counted from the observations described in (A). Different lowercase letters denote significant differences based on Tukey's test ($P < 0.05$). Values are means ±SE ($n = 4$–5). (C) Biochemical detection of autophagy flux for chloroplast stroma based on a free RFP assay. RFP and cFBPase (loading control) were detected by immunoblotting of soluble protein extracts from leaves of WT, *drp5b*, *atg5*, and *atg7* plants accumulating RBCS-mRFP. Protein extracts from either untreated control leaves (cont) or leaves after 2 d of incubation in darkness (dark) were used. Total protein was detected by Coomassie Brilliant Blue (CBB) staining as a loading control. The filled arrowhead indicates RBCS-mRFP fusion, and the open arrowhead indicates free mRFP derived from the cleavage of RBCS-mRFP. (D) Quantification of the free mRFP/RBCS-mRFP ratio shown relative to that of untreated wild-type plants, which was set to

1. Asterisks denote significant differences based on *t*-test (***, $P < 0.001$; n.s., not significant). Values are means ±SE ($n = 4$). Dots represent individual data points in each graph.

Figure 8–figure supplement 1. Production of Rubisco-containing bodies in *drp5b* mutants is ATG5-dependent.
(A) Confocal images of mesophyll cells from wild-type (WT), *atg5*, *drp5b*, and *drp5b atg5* leaves accumulating the stroma marker CT-GFP. Second rosette leaves were incubated in sugar-free solution containing 1 μM concanamycin A (concA) in darkness. Second rosette leaves from untreated plants were used as control. Green, CT-GFP; magenta, chlorophyll fluorescence. Only the merged channels are shown. Small vesicles containing CT-GFP without chlorophyll signal appear as green and are RCBs in the vacuole. Scale bars, 10 μm. (B) Number of accumulated RCBs, counted from the observations described in (A). Different lowercase letters denote significant differences based on Tukey's test ($P < 0.05$). Values are means ±SE ($n = 5$). Dots represent individual data points.

Figure 8–figure supplement 2. Vacuolar accumulation of stromal marker proteins in sugar-starved leaves.
(A) Confocal images of mesophyll cells from wild-type (WT), *drp5b*, *atg5*, and *atg7* leaves accumulating the stroma marker RBCS-mRFP. The leaves were incubated in sugar-free solution in darkness for 2 d. Second rosette leaves from untreated plants are shown as control. Green, RBCS-mRFP; magenta, chlorophyll fluorescence. Scale bars, 20 μm. (B) RFP intensity in the vacuolar lumen, as measured from the observations described in (A) and shown relative to that of untreated WT plants, which was set to 1. Asterisks denote significant differences based on *t*-test (***, $P < 0.001$; n.s., not significant). Values are means ±SE ($n = 4$). Dots represent individual data points.

Figure 9. Formation and segmentation of chloroplast buds in leaves of the *drp5b* mutant.
(A) A leaf from the *drp5b* mutant accumulating the stroma marker RBCS-mRFP was incubated in sugar-free solution in darkness and then observed. Arrowheads indicate a chloroplast bud. Green, RBCS-mRFP; magenta, chlorophyll fluorescence (Chl). (B) A leaf from the *drp5b* mutant accumulating the stroma marker RBCS-mRFP and the isolation membrane marker GFP-ATG8a were incubated in sugar-free solution in darkness and then observed. Arrowheads indicate the position of the chloroplast-associated isolation membrane. White or blue arrowheads indicate different isolation-membrane-associated sites in a chloroplast, respectively. Green, GFP-ATG8a; magenta, RBCS-mRFP; orange, chlorophyll fluorescence (Chl). Scale bars, 5 μm.

Video 13. Release of a chloroplast bud in a sugar-starved leaf of the *drp5b* mutant.
A leaf from the *drp5b* mutant accumulating the chloroplast stroma marker RBCS-mRFP was incubated in sugar-free solution in darkness for time-lapse imaging. Images acquired every 1.0 sec are displayed at 20 frames/sec. Scale bar, 5 μm. Green, RBCS-mRFP; magenta, chlorophyll fluorescence. Only the video of the merged channels is shown. This video was used to generate Figure 9A.

Video 14. A large chloroplast caused by the *drp5b* mutation forms RCBs along the isolation-membrane-associated sites.
A leaf from the *drp5b* mutant accumulating the chloroplast stroma marker RBCS-mRFP and the isolation membrane marker GFP-ATG8a was incubated in sugar-free solution in darkness for time-lapse imaging. Images acquired every 2.0 sec are displayed at 20 frames/sec. Scale bar, 5 μm. Green, GFP-ATG8a; magenta, RBCS-mRFP. Only the video of the merged channels is shown. This video was used to generate Figure 9B.

References

Abeliovich H, Zarei M, Rigbolt KTG, Youle RJ, Dengjel J (2013) Involvement of mitochondrial dynamics in the segregation of mitochondrial matrix proteins during stationary phase mitophagy. Nat Commun **4:** 2789

Caplan JL, Kumar AS, Park E, Padmanabhan MS, Hoban K, Modla S, Czymmek K, Dinesh-Kumar SP (2015) Chloroplast stromules function during innate immunity. Dev Cell **34:** 45-57

Chakraborty S, Hill AL, Shirsekar G, Afzal AJ, Wang GL, Mackey D, Bonello P (2016) Quantification of hydrogen peroxide in plant tissues using Amplex Red. Methods **109:** 105-113

Chen C, MacCready JS, Ducat DC, Osteryoung KW (2018) The molecular machinery of chloroplast division. Plant Physiol **176:** 138-151

Chen YF, Culetto E, Legouis R (2022) The strange case of Drp1 in autophagy: Jekyll and Hyde? Bioessays **44:** e2100271

Chiba A, Ishida H, Nishizawa NK, Makino A, Mae T (2003) Exclusion of ribulose-1,5-bisphosphate carboxylase/oxygenase from chloroplasts by specific bodies in naturally senescing leaves of wheat. Plant Cell Physiol **44:** 914-921

Clough SJ, Bent AF (1998) Floral dip: a simplified method for Agrobacterium-mediated transformation of Arabidopsis thaliana. Plant J **16:** 735-743

Delaney TP, Uknes S, Vernooij B, Friedrich L, Weymann K, Negrotto D, Gaffney T, Gutrella M, Kessmann H, Ward E, Ryals J (1994) A central role of salicylic-acid in plant-disease resistance. Science **266:** 1247-1250

Doelling JH, Walker JM, Friedman EM, Thompson AR, Vierstra RD (2002) The APG8/12-activating enzyme APG7 is required for proper nutrient recycling and senescence in *Arabidopsis thaliana*. J Biol Chem **277:** 33105-33114

Farre JC, Subramani S (2016) Mechanistic insights into selective autophagy pathways: lessons from yeast. Nat Rev Mol Cell Bio **17:** 537-552

Fukuda T, Ebi Y, Saigusa T, Furukawa K, Yamashita SI, Inoue K, Kobayashi D, Yoshida Y, Kanki T (2020) Atg43 tethers isolation membranes to mitochondria to promote starvation-induced mitophagy in fission yeast. Elife **9:** e61245

Fukuda T, Furukawa K, Maruyama T, Yamashita SI, Noshiro D, Song C, Ogasawara Y, Okuyama K, Alam JM, Hayatsu M, Saigusa T, Inoue K, Ikeda K, Takai A, Chen L, Lahiri V, Okada Y, Shibata S, Murata K, Klionsky DJ, Noda NN, Kanki T (2023) The mitochondrial intermembrane space protein mitofissin drives mitochondrial fission required for mitophagy. Mol Cell **83:** 2045-2058 e2049

Giacomello M, Pyakurel A, Glytsou C, Scorrano L (2020) The cell biology of mitochondrial membrane dynamics. Nat Rev Mol Cell Bio **21:** 204-224

Hanson MR, Sattarzadeh A (2008) Dynamic morphology of plastids and stromules in angiosperm plants. Plant Cell Environ **31:** 646-657

He YL, Gao JY, Luo MQ, Gao CJ, Lin YS, Wong HY, Cui Y, Zhuang XH, Jiang LW (2022) VAMP724 and VAMP726 are involved in autophagosome formation in Arabidopsis thaliana. Autophagy **19:**1406-1423

Hirota T, Izumi M, Wada S, Makino A, Ishida H (2018) Vacuolar protein degradation via autophagy provides substrates to amino acid catabolic pathways as an adaptive response to sugar starvation in *Arabidopsis thaliana*. Plant Cell Physiol **59:** 1363-1376

Ishida H, Izumi M, Wada S, Makino A (2014) Roles of autophagy in chloroplast recycling. Biochim Biophys Acta **1837:** 512-521

Ishida H, Okashita Y, Ishida H, Hayashi M, Izumi M, Makino A, Bhuiyan NH, van Wijk KJ (2021) GFS9 Affects Piecemeal Autophagy of Plastids in Young Seedlings of Arabidopsis thaliana. Plant Cell Physiol **62:** 1372-1386

Ishida H, Yoshimoto K, Izumi M, Reisen D, Yano Y, Makino A, Ohsumi Y, Hanson MR, Mae

T (2008) Mobilization of rubisco and stroma-localized fluorescent proteins of chloroplasts to the vacuole by an ATG gene-dependent autophagic process. Plant Physiol **148:** 142-155

Ishida H, Yoshimoto K (2008) Chloroplasts are partially mobilized to the vacuole by autophagy. Autophagy **4:** 961-962

Itakura E, Kishi-Itakura C, Mizushima N (2012) The hairpin-type tail-anchored SNARE Syntaxin 17 targets to autophagosomes for fusion with endosomes/lysosomes. Cell **151:** 1256-1269

Ito E, Uemura T (2022) RAB GTPases and SNAREs at the trans-Golgi network in plants. J Plant Res **135:** 389–403

Izumi M, Hidema J, Wada S, Kondo E, Kurusu T, Kuchitsu K, Makino A, Ishida H (2015) Establishment of monitoring methods for autophagy in rice reveals autophagic recycling of chloroplasts and root plastids during energy limitation. Plant Physiol **167:** 1307-1320

Izumi M, Ishida H, Nakamura S, Hidema J (2017) Entire photodamaged chloroplasts are transported to the central vacuole by autophagy. Plant Cell **29:** 377-394

Izumi M, Wada S, Makino A, Ishida H (2010) The autophagic degradation of chloroplasts via rubisco-containing bodies is specifically linked to leaf carbon status but not nitrogen status in Arabidopsis. Plant Physiol **154:** 1196-1209

Kohler RH, Cao J, Zipfel WR, Webb WW, Hanson MR (1997) Exchange of protein molecules through connections between higher plant plastids. Science **276:** 2039-2042

Kusano S, Nakamura S, Izumi M, Hagihara S (2023) A fluorescent molecular probe for live-cell imaging of starch granules. ChemRxib

Law SR, Chrobok D, Juvany M, Delhomme N, Linden P, Brouwer B, Ahad A, Moritz T, Jansson S, Gardestrom P, Keech O (2018) Darkened leaves use different metabolic strategies for senescence and survival. Plant Physiol **177:** 132-150

Mae T, Kai N, Makino A, Ohira K (1984) Relation between ribulose bisphosphate carboxylase content and chloroplast number in naturally senescing primary leaves of wheat. Plant Cell Physiol **25:** 333-336

Makino A, Osmond B (1991) Effects of nitrogen nutrition on nitrogen partitioning between chloroplasts and mitochondria in pea and wheat. Plant Physiol **96:** 355-362

Martinoia E, Heck U, Dalling MJ, Matile P (1983) Changes in chloroplast number and chloroplast constituents in senescing barley leaves. Biochem Physiol Pfl **178:** 147-155

Matsui T, Jiang PD, Nakano S, Sakamaki Y, Yamamoto H, Mizushima N (2018) Autophagosomal YKT6 is required for fusion with lysosomes independently of syntaxin 17. J Cell Biol **217:** 2633-2645

Miyagishima SY, Froehlich JE, Osteryoung KW (2006) PDV1 and PDV2 mediate recruitment of the dynamin-related protein ARC5 to the plastid division site. Plant Cell **18:** 2517-2530

Mochida K, Oikawa Y, Kimura Y, Kirisako H, Hirano H, Ohsumi Y, Nakatogawa H (2015) Receptor-mediated selective autophagy degrades the endoplasmic reticulum and the nucleus. Nature **522:** 359-362

Mochida K, Otani T, Katsumata Y, Kirisako H, Kakuta C, Kotani T, Nakatogawa H (2022) Atg39 links and deforms the outer and inner nuclear membranes in selective autophagy of the nucleus. J Cell Biol **221:** e202103178

Nakagawa T, Suzuki T, Murata S, Nakamura S, Hino T, Maeo K, Tabata R, Kawai T, Tanaka K, Niwa Y, Watanabe Y, Nakamura K, Kimura T, Ishiguro S (2007) Improved Gateway binary vectors: high-performance vectors for creation of fusion constructs in transgenic analysis of plants. Bioscience, biotechnology, and biochemistry **71:** 2095-2100

Nakamura S, Hagihara S, Izumi M (2021a) Mitophagy in plants. BBA-Gen Subjects **1865:** 129916

Nakamura S, Hagihara S, Otomo K, Ishida H, Hidema J, Nemoto T, Izumi M (2021b) Autophagy contributes to the quality control of leaf mitochondria. Plant Cell Physiol **62:** 229–247

Nakamura S, Hidema J, Sakamoto W, Ishida H, Izumi M (2018) Selective elimination of membrane-damaged chloroplasts via microautophagy. Plant Physiol **177:** 1007-1026

Nakamura S, Izumi M (2018) Regulation of chlorophagy during photoinhibition and senescence: lessons from mitophagy. Plant Cell Physiol **59:** 1135-1143

Nakatogawa H (2020) Mechanisms governing autophagosome biogenesis. Nat Rev Mol Cell Bio **21:** 439-458

Oikawa K, Goto-Yamada S, Hayashi Y, Takahashi D, Kimori Y, Shibata M, Yoshimoto K, Takemiya A, Kondo M, Hikino K, Kato A, Shimoda K, Ueda H, Uemura M, Numata K, Ohsumi Y, Hara-Nishimura I, Mano S, Yamada K, Nishimura M (2022) Pexophagy suppresses ROS-induced damage in leaf cells under high-intensity light. Nat Commun **13:** 7493

Onishi M, Yamano K, Sato M, Matsuda N, Okamoto K (2021) Molecular mechanisms and physiological functions of mitophagy. EMBO J **40:** e104705.

Ono Y, Wada S, Izumi M, Makino A, Ishida H (2013) Evidence for contribution of autophagy to rubisco degradation during leaf senescence in *Arabidopsis thaliana*. Plant Cell Environ **36:** 1147-1159

Osteryoung KW, Pyke KA (2014) Division and dynamic morphology of plastids. Annu Rev Plant Biol **65:** 443-472

Otomo K, Hibi T, Murata T, Watanabe H, Kawakami R, Nakayama H, Hasebe M, Nemoto T (2015) Multi-point scanning two-photon excitation microscopy by utilizing a high-peak-power 1042-nm laser. Anal Sci **31:** 307-313

Phillips AR, Suttangkakul A, Vierstra RD (2008) The ATG12-conjugating enzyme ATG10 is essential for autophagic vesicle formation in *Arabidopsis thaliana*. Genetics **178:** 1339-1353

Pyke KA, Leech RM (1994) A Genetic-Analysis of Chloroplast Division and Expansion in *Arabidopsis thaliana*. Plant Physiol **104:** 201-207

Rambold AS, Kostelecky B, Elia N, Lippincott-Schwartz J (2011) Tubular network formation protects mitochondria from autophagosomal degradation during nutrient starvation. Proc Natl Acad Sci U S A **108:** 10190-10195

Sasaki T, Tsutsumi M, Otomo K, Murata T, Yagi N, Nakamura M, Nemoto T, Hasebe M, Oda Y (2019) A novel katanin-tethering machinery accelerates cytokinesis. Curr Biol **29:** 4060-+

Segami S, Makino S, Miyake A, Asaoka M, Maeshima M (2014) Dynamics of vacuoles and H+-pyrophosphatase visualized by monomeric green fluorescent protein in Arabidopsis: artifactual bulbs and native intravacuolar spherical structures. Plant Cell **26:** 3416-3434

Spitzer C, Li FQ, Buono R, Roschzttardtz H, Chung TJ, Zhang M, Osteryoung KW, Vierstra RD, Otegui MS (2015) The endosomal protein CHARGED MULTIVESICULAR BODY PROTEIN1 regulates the autophagic turnover of plastids in Arabidopsis. Plant Cell **27:** 391-402

Thompson AR, Doelling JH, Suttangkakul A, Vierstra RD (2005) Autophagic nutrient recycling in Arabidopsis directed by the ATG8 and ATG12 conjugation pathways. Plant Physiol **138:** 2097-2110

Tsuboyama K, Koyama-Honda I, Sakamaki Y, Koike M, Morishita H, Mizushima N (2016) The ATG conjugation systems are important for degradation of the inner autophagosomal membrane. Science **354:** 1036-1041

Twig G, Elorza A, Molina AJA, Mohamed H, Wikstrom JD, Walzer G, Stiles L, Haigh SE, Katz S, Las G, Alroy J, Wu M, Py BF, Yuan J, Deeney JT, Corkey BE, Shirihai OS (2008) Fission and selective fusion govern mitochondrial segregation and elimination by

autophagy. EMBO J **27:** 433-446

Vitha S, Froehlich JE, Koksharova O, Pyke KA, van Erp H, Osteryoung KW (2003) ARC6 is a J-domain plastid division protein and an evolutionary descendant of the cyanobacterial cell division protein Ftn2. Plant Cell **15:** 1918-1933

Wada S, Ishida H, Izumi M, Yoshimoto K, Ohsumi Y, Mae T, Makino A (2009) Autophagy plays a role in chloroplast degradation during senescence in individually darkened leaves. Plant Physiol **149:** 885-893

Wang WH, Li JY, Sun QQ, Yu XY, Zhang WW, Jia N, An CJ, Li YQ, Dong YN, Han FJ, Chang N, Liu XM, Zhu ZL, Yu Y, Fan SL, Yang MJ, Luo SZ, Gao HB, Feng Y (2017) Structural insights into the coordination of plastid division by the ARC6-PDV2 complex. Nat Plants **3:** 17011

Weaver LM, Amasino RM (2001) Senescence is induced in individually darkened Arabidopsis leaves but inhibited in whole darkened plants. Plant Physiol **127:** 876-886

Yamashita S, Jin XL, Furukawa K, Hamasaki M, Nezu A, Otera H, Saigusa T, Yoshimori T, Sakai Y, Mihara K, Kanki T (2016) Mitochondrial division occurs concurrently with autophagosome formation but independently of Drp1 during mitophagy. J Cell Biol **215:** 649-665

Yoshimoto K, Hanaoka H, Sato S, Kato T, Tabata S, Noda T, Ohsumi Y (2004) Processing of ATG8s, ubiquitin-like proteins, and their deconjugation by ATG4s are essential for plant autophagy. Plant Cell **16:** 2967-2983

Yoshimoto K, Jikumaru Y, Kamiya Y, Kusano M, Consonni C, Panstruga R, Ohsumi Y, Shirasu K (2009) Autophagy negatively regulates cell death by controlling NPR1-dependent salicylic acid signaling during senescence and the innate immune response in *Arabidopsis*. Plant Cell **21:** 2914-2927

Yoshimoto K, Ohsumi Y (2018) Unveiling the molecular mechanisms of plant autophagy-from autophagosomes to vacuoles in plants. Plant Cell Physiol **59:** 1337-1344